Inventory of large landslides along the Central Western Andes (ca. 15°–20° S): Landslide distribution patterns and insights on controlling factors

Fabrizio Delgado [a,b], Swann Zerathe [b,*], Stéphane Schwartz [b], Bastien Mathieux [b], Carlos Benavente [a,c]

[a] *Especialidad Ingeniería Geológica, Facultad de Ciencias e Ingeniería. Pontificia Universidad Católica del Perú, Av. Universitaria 1801, San Miguel, Lima, 15088, Peru*
[b] *Univ. Grenoble Alpes, Univ. Savoie Mont Blanc, CNRS, IRD, IFSTTAR, ISTerre, 38000, Grenoble, France*
[c] *Instituto Geológico, Minero y Metalúrgico INGEMMET, Av. Canadá, 1470, Lima, Peru*

ARTICLE INFO

ABSTRACT

The western flank of the Central Andes hosts some of the largest terrestrial landslides ($v > km^3$), which morphologies are particularly well-preserved due to low erosion rates related to the hyper-arid climate prevailing in this region since the Miocene. First-order questions are pending about the factors controlling the development and the triggering of those large-scale slope failures. Previous studies provided some geomorphological analysis and dating on individual study cases, but a regional-scale vision of landslide processes long the Central Western Andes is missing.

Here we report an original inventory of large landslides (areas from 0.1 to 180 km^2) established along the western flank of the Central Andes between latitudes ca. 15 and 20° S, and from the Pacific coast to the Altiplano. Based on manual mapping (using satellite images analysis, Google Earth and DEMs analysis) and a compilation of previous works, we inventoried more than a thousand large landslides in this region. We then statistically explored the database according to the landslides typology, size, abundance and relation to geologic, tectonic and climatic settings of the Central Western Andes in order to provide a first insight on their controlling factors. Landslide size-frequency distribution follows a power-law with an exponent of 2.31 ± 0.16 and a cut-off of 4.0 ± 1.9 km^2 showing a strong contribution of the largest landslides to the cumulated landslide area. We revealed a dominance of rockslide typology (86%) characterized by in-mass slides, the rest being rock-avalanche type (14%) marked by typical granular-flow morphologies. Combination of specific lithology and great local relief emerge as favorable conditioning factor for large landslide initiation, in particular in the case of river incisions though ignimbrites of the Paleogene-Neogene (Huaylillas Formation), concentrating >30% of the landslides. Moreover, landslide clusters tend to follow crustal faults networks suggesting a long-term control of tectonic activity. Most of the identified landslides are paleo events. We tentatively argue that their triggering could not have been possible in the current hyper-arid conditions of the Atacama Desert and its periphery. Future research providing dating on some of the landslide clusters identified in this study is needed to explore possible temporal correlations between periods of landslide activity and external seismic and/or climatic cycles.

1. Introduction

Landslides are ubiquitous gravity phenomena on Earth, found in any environment with slopes. Their triggering is conditioned by the internal mechanical and hydrological properties of geomaterials (Guzzetti et al., 1996; Stead and Wolter, 2015), and may depend on external factors associated with seismotectonic activity (Fan et al., 2019) or climatic variations (Pánek, 2019). They constitute one of the major sources of hazard, responsible for thousands of victims and billions of dollars in damages each year (Petley, 2012; Froude and Petley, 2018; Wallemacq and House, 2018). The constant growth of the world population associated with the ongoing climate changes are factors that may severely increase the level of risk and hazard related to landslide activity (Gariano et Gariano and Guzzetti, 2016; Haque et al., 2019). In this context, a better understanding of landslide processes and their causative factors is crucial and those questions have received a growing interest (Wu

---

* Corresponding author.
E-mail address: swann.zerathe@ird.fr (S. Zerathe).

et al., 2015). On longer timescales, landslides are recognized as the main erosional process in orogenic zones (e.g. Korup et al., 2007). Landslide rate is thought to mirror the long-term trend of tectonic uplift, landsliding continuously affecting steep slopes along the valley flanks of incising rivers (Larsen and Montgomery, 2012). Doing so, landslides are the main agent transporting material from hillslopes to rivers and limiting the elevation and the relief construction in mountain ranges (Whipple et al., 1999; Montgomery, 2001; Roering, 2012).

To disentangle hazard issues and to progress toward a better understanding of landslides processes, research strategies based on landslide inventories have shown interesting potential (Malamud et al., 2004; Guzzetti et al., 2012). Numerous landslide inventories have been built after single storm events or strong earthquakes, using remote sensing approaches to detect the triggered landslides (see reviews in Marc et al. (2018) and Tanyaş et al. (2017), for rainfall-induced and earthquake-induced landslide inventories, respectively). Providing statistics on landslide processes, those inventories can highlight specific patterns and reveal generic landslide properties, such as the earthquake-induced landslide size decreasing with distance from the fault trace (Valagussa et al., 2019), the control of relief on landslide size (Medwedeff et al., 2020) or the influence of total rainstorm on the proportion of large landslides (Marc et al., 2018). However, deciphering landslides patterns on a longer time scale (hundreds to thousands of years) and at a large spatial scale is more complex because erosion continuously removes the geomorphological evidence of past events. Furthermore, automatic detection of past landslides in landscapes is not efficient at present-day and establishing paleo landslides inventory requires a manual mapping based on expert vision (e.g. Pánek et al., 2019; Görum, 2019). Those inventories allow to understand the relations between large landslides and relief properties at an orogenic scale and to unravel the respective effects of long-term seismotectonic activity and Quaternary climate changes on slope instabilities.

In this study, we focus on large landslides along the western flank of the Central Andes between ca. 15° and 20°S, in both south Peru and north Chile, and we aim at establishing a comprehensive inventory of landslides in this area. This region is an atypical place for several aspects. First, it is particularly active geodynamically, related to the long-term convergence between the Nazca and the South America plates (Armijo et al., 2015; Martinod et al., 2020). This global shortening generates relief construction (Martinod et al., 2020) and produces instantaneous deformation (subduction and crustal seismicity; Villegas-Lanza et al., 2016) coupled with long-term processes of surface uplift (Thouret et al., 2017) and volcanism (Mamani et al., 2009). Second, the climate of this region is specific, with some places being one the driest worldwide: referred to as the Atacama Desert in Northern Chile and Southern Peru (Hartley and Chong, 2002). This desert, where a hyper-arid climate has been maintained for several millions of years (e. g. Hartley and Chong, 2002; Dunai et al., 2005) is often referred to as a Martian proxy (Valdivia-Silva et al., 2011; Irwin et al., 2014). The long-term aridity is responsible for very low erosion and weathering rates (1–10 mm kyr^{-1}; Nishiizumi et al., 2005), allowing for exceptionally long preservation of landscapes and offering a unique time window to study slope instabilities at geological time scales. At the same time, strong storms can episodically occur during El Niño event. Finally, the western flank of the Central Andes hosts some of the largest landslides ever identified on the emerged Earth surface (e.g. Chuquibamba (Margirier et al., 2015), Caquilluco (Crosta et al., 2015), Lluta (Strasser and Schlunegger, 2005), mobilizing volumes of several cubic kilometers, with kilometric long run-outs, similar to those reported on the Mars surface (Lucas et al., 2014). Some previous studies have been conducted on those individual slope failures, revealing that the instabilities are ancient with ages ranging from tens to hundreds of thousands of years (Zerathe al., 2017; Crosta et al., 2017; Delgado et al., 2020; Sánchez-Núñez et al., 2020). However, questions remain about the link between those landslides and the conditioning factors along the Central Western Andes and also with the seismicity and the past climate variations in this region. Other preliminary works have revealed that much more large landslides may exist there (Audin and Bechir, 2006; Mather et al., 2014; Crosta et al., 2014) but a general view of the distribution of the landslide activity at the scale of the Central Western Andes instabilities is missing.

The scope of the paper is to establish a landslide inventory as exhaustive as possible along the northermost Central Western Andes (ca. 15° - 20°S), our strategy was based on a review of previous works on landslides existing in the literature for this region and on an original mapping of unrecognized large landslides based mainly on satellite images, Google Earth and DEMs analysis. The finalities of this study are: (1) to provide an updated database of large landslides existing between latitudes ca. 15 and 20°S. This database will be open and may be modifiable; (2) to provide a first-order view of their typology, size, abundance and distribution; and (3) to search for statistical patterns between landslide distribution and background settings in order to better understand their conditioning factors.

2. Settings of the western flank of the Central Andes

2.1. Geodynamic and large-scale morphology

The Andean cordillera is located on an active tectonic margin where the subduction of the Nazca plate beneath the South American plate occurs since ~50 Ma (Pardo-Casas and Molnar, 1987) with a convergence rate of ~62 mm. yr^{-1} (Villegas-Lanza et al., 2016). This process generates the construction of the Andes and leads to the formation of successive volcanic arcs. Their locations varied in time and were controlled by the change of the dip of the subduction slab (Isacks, 1988; Allmendinger et al., 1997; James and Sacks, 1999; Sobolev and Babeyko, 2005; Haschke et al., 2006; Mamani et al., 2008, 2009). This dynamic produced long-term crustal thickening controlled by magmatic underplating and tectonic shortening. The western flank of the Central Andes is classically subdivided into three main areas (Fig. 1) based on different geological and morphological settings inherited from the long-term geodynamics evolution of the Andes.

The first area corresponds to the Coastal Cordillera (CC) which is mainly characterized by Proterozoic craton (so-called the Arequipa massif, Cobbing and Pitcher, 1972) represented by the association of gneisses and migmatites which have been later intruded by Paleozoic plutons (Cobbing and Pitcher, 1972; Cobbing et al., 1977; Mukasa and Henry, 1990). This Coastal Cordillera forms currently a narrow band reaching 50-km-wide and moderate relief and elevation up to 1000 m a. s.l. along the Pacific coastline.

The second area corresponding to the Central Depression (CD) exhibits Tertiary sedimentary series, the so-called Moquegua formation, unconformably resting above the Proterozoic and Paleozoic bedrock. This area corresponds to a flexural depression located in the front of the volcanic arc. This basin collected the erosional products of the Andean relief under construction. Those detrital sedimentary series can be locally more than 1-km thick (Roperch et al., 2006; Thouret et al., 2007; Schildgen et al., 2007; Garzione et al., 2008). Their lithologies evolve from thin marine sequences at the base toward conglomeratic continental deposits with interstratified ignimbrites levels at their top. At present-day, this area forms a pediment plain, almost flat with mean elevations ranging from 1000 to 1500 m a.s.l., and locally affected by fluvial incision (Thouret et al., 2007; Schildgen et al., 2007; Garzione et al., 2008).

The third area corresponds to the Western Cordillera (WC) which presents a higher relief from 1000 to 5000 m a.s.l. It is made of Mesozoic marine sequences and Cenozoic, essentially Paleogene-Neogene, volcano-sedimentary series related to the migration of the successive volcanic arcs (Mamani et al., 2010). One of the last main volcanic phases corresponds to the so-called Huayllillas arc (24-10 Ma, Quang et al., 2005; Thouret et al., 2007). It produced thick ignimbrite deposits (up to 300 m of thickness) at a regional scale. Along the Western Cordillera, the
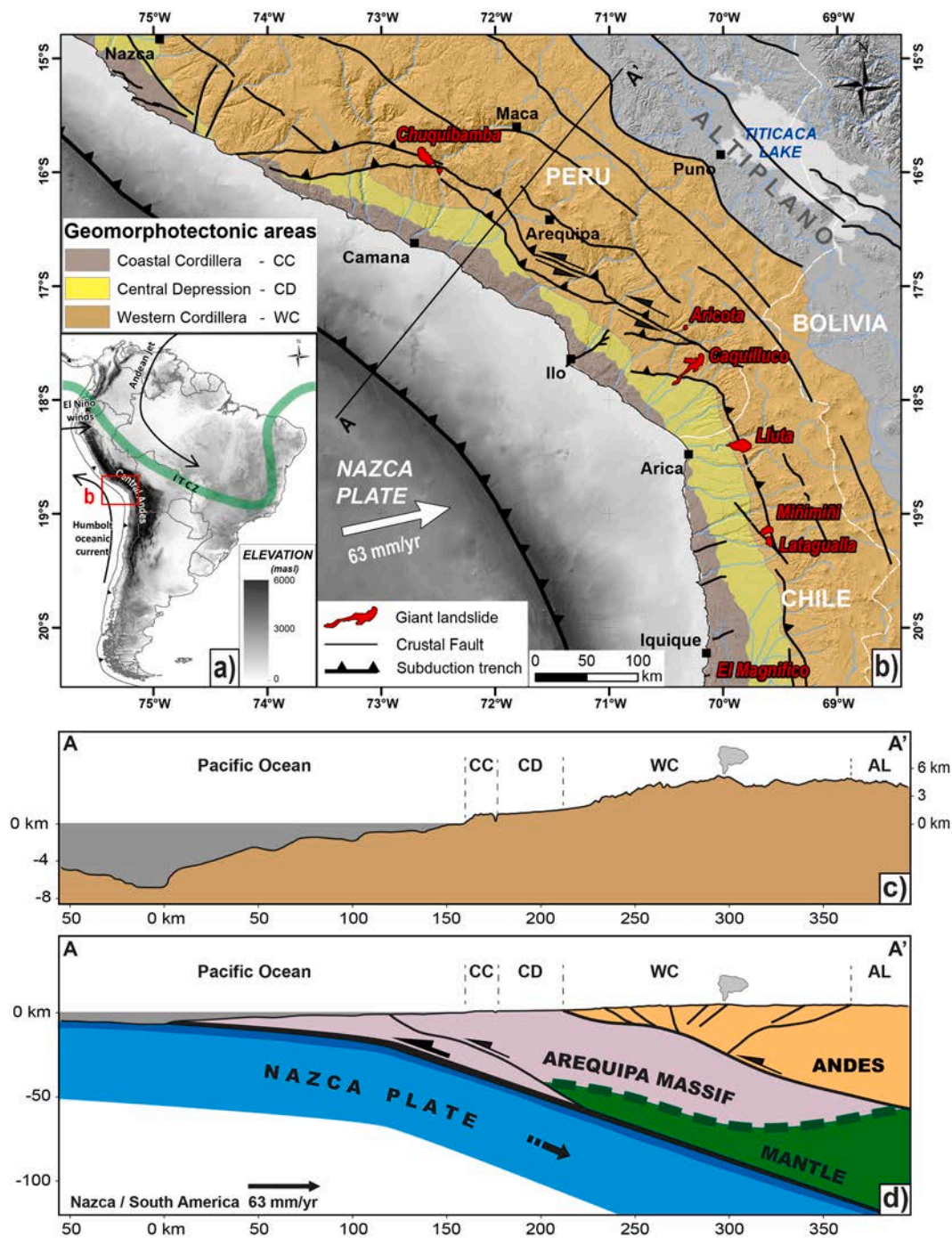
Fig. 1. (a) Study area location and major climatic features of South America showing the Intertropical Convergence Zone (ITCZ), El Niño wings and the Humboldt oceanic current, (b) focus on the study area showing the different geomorphotectonic areas of the Central Western Andes and the location of giant landslides documented in the literature (Chuquibamba landslide - Margirier et al., 2015; Thouret et al., 2017; Aricota landslide - Delgado et al., 2020; Caquilluco landslide - Zerathe et al., 2017; Lluta landslide - Wörner et al., 2002; Strasser and Schlunegger, 2005; Miñimiñi and Latagualla landslides - Pinto et al., 2008; El Magnifico landslide - Mather et al., 2014; Crosta et al., 2017), (c) and (d) AA′ topographic profile of the western flank of the Central Andes and its geological interpretation (adapted from Armijo et al., 2015), respectively. CC: Coastal Cordillera, CD: Central Depression, WC: Western Cordillera, AL: Altiplano.

top of the Huaylillas deposits corresponds to a preserved paleosurface used as a reference surface at a regional scale. All this domain is affected by tectonic shortening associated with the development of large-scale anticline geometry, well underline by flexures of the Huaylillas paleosurface, and by pluri-kilometric crustal fault systems.

As previously introduced, among those three sub-areas, the Western Cordillera is the region where some of the largest landslides have been reported in the literature (Chuquibamba landslide - Margirier et al., 2015; Thouret et al., 2017; Aricota landslide - Delgado et al., 2020;

Caquilluco landslide - Zerathe et al., 2017; Lluta landslide - Wörner et al., 2002; Strasser and Schlunegger, 2005; Miñimiñi and Latagualla landslides - Pinto et al., 2008; El Magnifico landslide - Mather et al., 2014; Crosta et al., 2017, Fig. 1). We bring here below further detailed geological and geomorphological descriptions of this key region required to better understand the gravitational destabilization affecting the Central Western Andes.

2.2. Lithostratigraphy

The oldest rocks in the studied area correspond to the Precambrian crystalline basement. It consists of gneiss, migmatites, pegmatites, schists and diorites. This rock assemblage is located between latitudes 15°-18°S, outcropping mainly along the Peruvian Coastal Cordillera along an NW-SE orientation (Fig. 2) and was dated between 1861 ± 32 Ma and 946 Ma by Casquet et al. (2010).

Paleozoic rocks were emplaced in erosional unconformity, their lithostratigraphic units are observed along the Coastal Cordillera (Fig. 2) and are represented by the Marcona (Cambrian), Cabanillas (Devonian), Ambo and Tarma (Carboniferous) formations. These units are mostly made up of limestones, conglomerates, sandstones and shales (Newell, 1945).

The Mesozoic record is characterized by important Jurassic and Cretaceous marine sedimentation, controlled by the tectonic opening of the Arequipa-Tarapacá sedimentary basin (Vicente, 1981). Those deposits outcrop all along the entire western Andean flank and correspond to thick series of limestones (mudstone to grainstone) and marls of the Pelado and Socosani formations (Wilson and García, 1962; Monge and Cervantes, 2000) conformably covered by the Yura Group and the Hualhuani Formation (Wilson and García, 1962; Vicente, 1981) composed of quartz sandstones and black shales interstratified. The top of the Mesozoic series is affected by an erosive discordance, overlain by volcanic and volcano-sedimentary rocks of the Toquepala Group (Bellido Bravo and Guevara, 1963; Bellon and Lefevre, 1916).

The distribution of the Cenozoic lithostratigraphic units is more complex and is related to the formation of the volcanic arc of the Andes, its successive migration and its importance in the creation of forearc, back-arc and intra-arc basins. In the Coastal Depression, deposits of sedimentary sequences accumulated, mainly of marine origin, also from the erosion coming from the proto-Andean under construction, which generated the almost synchronous creation of the Camaná and Moquegua basins in southern Peru and Azapa in northern Chile. These interstratified sequences of conglomerates with volcanic sequences are called Moquegua Group (Thouret et al., 2007; Schildgen et al., 2007) in Peru while in Chile they correspond to the Azapa Formation (Wörner et al., 2000; Pinto et al., 2007). These sequences, which are up to 800 m thick (Bellido, 1979), are the result of erosion of the Western Cordillera and were deposited from the Oligocene to the late Miocene. From the Eocene onwards, constant volcanic events began and continue to the present day. The Huaylillas formation (Wilson and García, 1962), constitutes a wide surface that extends up to the north of Chile, where it is called Huaylillas surface (Wörner et al., 2000). This formation is a stratigraphic superposition of pyroclastic flows (Wörner et al., 2000; Mamani et al., 2010) developing a thickness between 500 and 600 m (Wilson and García, 1962; Salinas, 1985). This formation is well-preserved due to the hyper-arid climatic conditions and its top surface represents a regional paleosurface. The only forms of erosion are the incision of the valleys produced by the rivers descending from the Altiplano (Evenstar et al., 2017). The northeast is dominated by a large volume of andesites and rhyolites associated with ignimbrites assigned to the Barroso Group (Roperch et al., 2006; Mamani et al., 2010; Acosta et al., 2011), related to the magmatic activity of the Barroso Arc (Mamani et al., 2012). The Quaternary rocks are expressed by Pleistocene lava produced during a recent activity of active volcanoes (e.g. Sabancaya, Ampato, Ubinas) related to the activity of the magmatic arc (e.g. Mariño et al., 2021; Rivera et al., 2020). Quaternary deposits cover a large part of the basement and can reach a few meters thick. These deposits correspond to fluvial and alluvial deposits in the main valley and glacial deposits in high elevation areas that evidence recent climatic fluctuations.
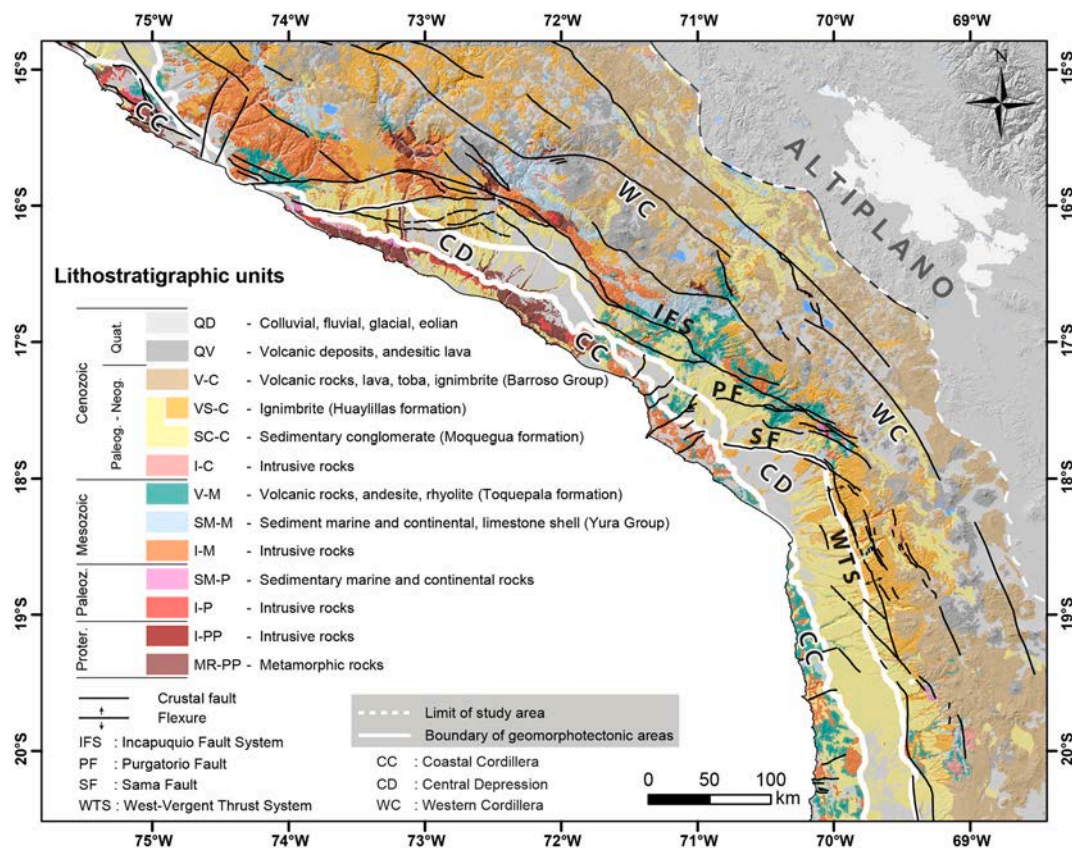

Fig. 2. Lithostratigraphy and main structural features of the Central Western Andes (adapted from http://geocatmin.ingemmet.gob.pe/geocatmin for Peru and https://portalgeominbeta.sernageomin.cl/ for Chile).

2.3. Tectonic setting

Active or neotectonic faults are mostly present along the Western Cordillera area (http://neotec-opendata.com; http://geocatmin.ingemmet.gob.pe/geocatmin). The width of the Western Cordillera shows important variations being wider in South Peru than along North Chile (Fig. 1). This variation is related to the partitioning of the deformation controlled by the Nazca plate convergence toward a curved shape boundary (Arica bend) of the South American plate (Allmendinger et al., 1997). The Western Cordillera is deformed by intense folding, inverse faults and large overflows due to the shortening and thickening of the crust mainly associated with an increase in the subducted slab angle (Armijo et al., 2015).

In southern Peru, the tectonic regime is transpressive related to the activity of the Incapuquio Fault System (IFS), which extends for more than 200 km along an NW-SE direction (Fig. 2). This crustal-scale fault system displays sinistral displacement affecting mainly the Moquegua Formation and the Toquepala and Yura groups, defining a tectonic contact between them (Jacay et al., 2002). The IFS is considered potentially active as shown by the paleo-seismological studies that revealed Holocene surface ruptures (Benavente et al., 2021). Other secondary fault systems are connected to the IFS such as: (i) the Purgatorio fault (PF), located between the Pampa Purgatorio and the village of Mirave, striking E-W along 70 km (Benavente et al., 2017b) or (ii) the Sama-Calientes fault (SF), striking E-W along ~50 km (Hall et al., 2008). Both are mainly reverse faults with a slight dextral component and have registered Holocene reactivations and surface failures (Benavente and Audin, 2009; Benavente et al., 2017b).

To the south of the Arica bend (in North of Chile) the tectonic regime becomes compressive and correlated with an important increase in the plate convergence during the last 30-20 Myr (Pardo-Casas and Molnar, 1987; Somoza, 1998). The most important structure corresponds to the West-Vergent Thrust System (WTS) located in the Western Cordillera (Fig. 2) with an N–S trending direction and extending over 450 km in northern Chile (García et al., 2004, 2013; Blanco and Tomlinson, 2013; Valenzuela et al., 2014; Morandé et al., 2015; Tomlinson et al., 2015). This main regional tectonic structure presents W-dipping high angle segments associated with the development of large folds with monoclinal geometry described as regional flexures. These structures present slight variations in the magnitude of displacement along the course
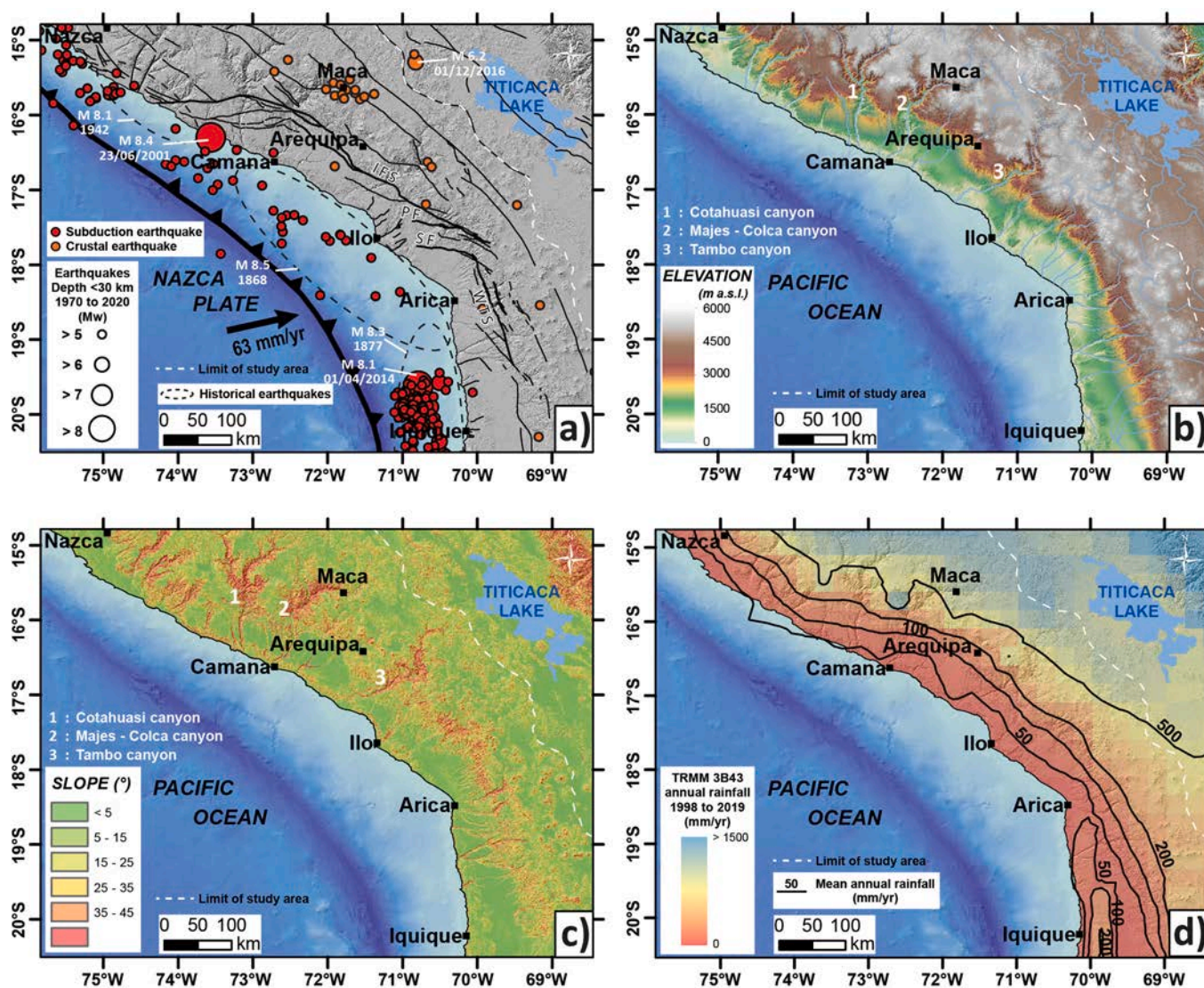

Fig. 3. Settings of the western flank of the Central Andes. (a) fault and seismicity (faults database: http://neotec-opendata.com and http://geocatmin.ingemmet.gob.pe/geocatmin; instrumental earthquakes from http://ds.iris.edu/seismon/index.phtml and historical earthquakes from Villegas-Lanza et al., 2016). (b) and (c) topography and slope, respectively (both derived from SRTM DEM of 30 m of resolution), (d) mean annual rainfall (TRMM 3B43 annual rainfall of the Andes averaged for the period of 1998–2019). The white dashed line marks the eastern limit of our study area.

(Pinto et al., 2004; Farías et al., 2005) and affect rocks of the Moquegua Group and the Huaylillas formation (ignimbrites).

2.4. Seismicity

The western flank of the Central Andes is affected by two types of seismic activity (Fig. 3a). The first one is related to the subduction dynamics that produce earthquakes with magnitudes that could be higher than 8, with slab ruptures of several hundreds of kilometers along the subduction zone (Villegas-Lanza et al., 2016). Recent strong subduction earthquakes include the 2007 Pisco earthquake (Mw 8.0, depth 18 km, ~100 km north to the study area), the 2001 Arequipa earthquake (Mw8.4; depth 30 km) and the 2014 Iquique earthquake (Mw8.1, depth 20 km) (Fig. 3d). Those earthquakes were also associated with swarms of seismicity and aftershocks of moderate to high magnitudes (Fig. 3a). Several historical mega earthquakes are also documented in this area (see Fig. 3a). A recurrence time between 100 and 300 years is proposed for those events for the same slab portion (Kelleher, 1972; Dorbath et al., 1990; Chlieh et al., 2011).

The second one is related to the crustal faults network. The Coastal Cordillera, Central Depression and the Western Cordillera are affected by several major faults (Figs. 2 and 3a) that experienced recent seismo-tectonic activity (Lavenu et al., 2000; Jacay et al., 2002; Audin et al., 2003, 2006; Barrientos et al., 2004; Lavenu, 2005; PMA, 2009; Leyton et al., 2010; Benavente et al., 2017a, 2017b). The seismic record in the study area is mainly focused on the subduction dynamics because it produces the strongest earthquakes. In contrast, the western cordillera does not benefit from a seismic network allowing the location of earthquakes at crustal-scale depth in relation to the major faults distribution (Figs. 2 and 3d). However, some seismic records over the last 50 years apart from the region of Maca (upper Colca) (Fig. 3a) have been reported that indicate moderate seismicity up to Mw5. Paleoseismological studies show that some of these faults have produced recurrent shallow seismicity during the Holocene. The analyses of the offsets along the rupture surfaces are consistent with earthquake magnitudes up to Mw7.5 (e.g. Benavente et al., 2017a; Santibáñez et al., 2019). These are some examples: the Incapuquio fault (Audin et al., 2008; Benavente et al., 2021), the Purgatorio fault (Benavente et al., 2017b), the Sama-Calientes fault (Audin et al., 2006) and the Bajo Molle fault (González et al., 2015). The length of fault failure is smaller compared to subduction earthquakes, but the energy and the ground acceleration generated by the shallow ruptures along those faults can be very strong (Benavente et al., 2017a). The recurrence period for this type of crustal seismicity is commonly assumed to be about thousand years (Leyton et al., 2010; Benavente et al., 2017b).

2.5. Topography

As shown by Fig. 3b and c, the western flank of the Central Andes is characterized by two main types of topography. First, a large wavelength topography that is directly related to the orogen formation and its evolution. This topography, with elevation ranges between 1500 and 4500 m a.s.l. forms the Western Andean flank itself, striking NW-SE in Peru and NNW-SSE in Chile, roughly parallel to the subduction trench (Fig. 3b). Steep slopes (20–30°) are found at the southern extremity of the Western Cordillera, along the main reverse faults and anticlinal-flexure growth (Fig. 3a). This large-scale wave-length topography is also revealed by a major paleosurface developed above the Huaylillas ignimbrite. This major geomorphological feature exists all along the western flank of the Central Andes (Fig. 2), characterized by a regular primitive drainage network forming a large striped surface. Its mean slope varies between 5° and 20° (mainly toward the South) depending on the local amplitude of the structural flexure and fault-propagation folds (Wilson and García, 1962). Second, a more local but stronger topography corresponds to the deep canyons that dissect the Western Cordillera. They are up to several kilometers deep in some places in

southern Peru (Cotahuasi, Majes, Tambo, see Fig. 3b and c), generating strong local relief and very steep slopes (>30°) along their flanks (Fig. 3c). The formation of those canyons started during the late Miocene and is related to the regional uplift and the specific climate of this region (Thouret et al., 2007; Schildgen et al., 2009, 2010; Gunnell et al., 2010).

2.6. Current and past climate

The Central Western Andes of southern Peru and northern Chile are part of the Atacama Desert, known as one of the driest places worldwide. Several factors are often proposed to explain this extreme lack of precipitation: (1) the mid-latitude of the region (~20°S) located along the sinking branch of the Hadley Circulation generating high pressure of dry air; (2) the oceanic Humboldt Current, characterized by upwelling of cold water along the South American Pacific coast, which cools the air near the surface and prevent moisture evaporation from the Pacific ocean (La Niña-like conditions); (3) the rain shadow effect of the Andes limiting the transfer of moisture coming from the Atlantic and the Amazonia (Houston and Hartley, 2003).

The main source of moisture is coming from the northeast, from the Atlantic Ocean and the Amazonian basin as depicted by a north-south rainfall gradient (Fig. 3d). Precipitations can reach ~1000 mm/yr in the northeastern boundary of our study area (at latitude ~15°S) and along the western boundary of the Central Altiplano (Fig. 3d). Those precipitations are seasonal, occurring mostly during the austral summer, associated with the South American monsoon regime and the seasonal southward shift of the Intertropical convergence zone above the Altiplano. Despite a little of this moisture can reach the upper part of the Pacific watersheds, the Western Cordillera, as part of the Atacama Desert, remains arid receiving less than 200 mm/yr of rain, while the coast and coastal depression receive less than 50 mm/yr of rain (New et al., 2002; Strecker et al., 2007). The hyper-aridity of the Atacama Desert, and such climatic setting, are thought to prevail since at least 10 Ma (Rech et al., 2019 and references therein), responsible for very low denudation rates over the long term (erosion<0.5 m/Ma; e.g. Hall et al., 2008; Placzek et al., 2013) and long-term preservation of landscapes. On the other hand, as the upper of the watersheds received precipitations from Amazonian moisture, the main rivers have strong erosional capacity which produced deep canyon incisions (Cotahuasi, Majes, Tambo; Fig. 3b and c) through the arid Western Cordillera.

The current meteorological conditions can be episodically modulated by El Niño Southern Oscillation (ENSO) which results in a warming of the Pacific Ocean surface related to the Trade winds carrying warm water from the eastern equatorial Pacific towards the South American coast. This can lead to very strong storms such as in March 2015, when up to 40 mm of 1-day accumulated precipitation fed the Atacama region (Bozkurt et al., 2016), triggering strong flash floods and debris flows (Aguilar et al., 2020). Despite paleoclimate records covering the Late Quaternary in the Atacama region being rare and often discontinuous (e. g. Bartz et al., 2020), some evidences of past humid phases has been also reported. They included widespread pluvial stages termed the Central Andean Pluvial Event (CAPE, e.g. Quade et al., 2008; Gayo et al., 2012) recorded as lake extensions and glacier advances in the Central Atacama of Northern Chile. Records of flash floods and debris flows linked to paleo-El Niño events have been reported during the late Pleistocene in Southern Peru (e.g. Keefer et al., 2003). Then evidences of more persistent humid conditions related to ENSO-like climate configuration during the last interglacial periods are recorded as paleolakes extensions (e.g. Ritter et al., 2018; Placzek et al., 2013) and fluvial terraces aggradation in the valleys (Steffen et al., 2010; Litty et al., 2016). Those humid events are thought to have persisted over millennial to plurimillenial periods (i.e. the Ouki Event (100–120 ka), Placzek et al., 2013; Ritter et al., 2019).

3. Methods

3.1. Landslide mapping strategy

Our main objective was to establish an inventory as exhaustive as possible of large landslides (areas >0.1 km^2) along the Central Western Andes in a region bounded to the north and south by the exact latitudes 14.8 and 20.5°S, and to the west and east by the Pacific coast and the western limit of the Altiplano, respectively (Fig. 1b). As detailed here below, our landslide inventory was based on: (1) a review of previous works and mapping of landslides existing in the literature for this region and (2) a manual mapping of newly recognized large landslides based on specific geomorphologic criteria combing GIS analysis (using Google Earth and DEMs (30 m TanDEM-X and 2 m Pleiades). This mapping using remote tools was made possible by the collective expertise of our team acquired during several past field works dedicated to landslide-geomorphology-tectonic in this region for a dozen years. About 10% of the landslides inventoried in this study were visited in the field, several of those being mapped in detail as already published in previous works involving our team (e.g. Zavala et al., 2013; Margirier et al., 2015; Zerathe et al., 2016, 2017; Delgado et al., 2020).

Indeed, the reviews of previous studies included individual landslide case studies (e.g. Strasser and Schlunegger, 2005; Pinto et al., 2008; Hermanns et al., 2012; Zavala et al., 2013; Margirier et al., 2015; Zerathe et al., 2016, 2017; Bontemps et al., 2018; Lacroix et al., 2015, 2019, 2020; Thouret et al., 2017; Delgado et al., 2020; Gaidzik et al., 2020; Sánchez-Núñez et al., 2020). We also revised a few studies including some local landslide databases such as (Audin and Bechir, 2006 and Crosta et al., 2014 for South Peru and Mather et al., 2014 and Crosta et al., 2014 for North Chile). Following this review, we note that two main types of landslide dominate in this region (Fig. 4): (i) coherent landslides for which the slipped mass moved in only one or few packets, typically corresponding to rockslide typology, and (ii) disrupted landslides which evolve as a granular flow of rock and boulders, typically corresponding to rock avalanche typology. In order to decipher if those two landslide types may have different controlling factors, we kept this binary classification for our mapping.

Fig. 4 illustrates the specific geomorphologic criteria that we used for mapping and classification for both cases. Importantly, a landslide phenomenon was ascribed to a site only if the formal identification of a headscarp associated to a slipped mass was possible. To the contrary, morphologies such as large erosional amphitheaters or slope-break were not mapped as a landslide if a slipped mass was not clearly identified at the scarp base. Finally, we attempted to define a qualitative state of activity for our mapped landslides, trying to distinguish between two main types (Fig. 4). First the recent or active landslides, that are known to affect human infrastructures (agricultural land, road, village, etc.), showing fresh morphologies (fresh scarp, recent river dam, etc.) and/or which are monitored and referred in published papers. Additionally, we attempted to revise each mapped landslide on the Google Earth time-lapse tools, to visually check if some surface large-scale displacements (>100 m) might occur in the last 37-years. The oldest images (from 1985 to ~2005) being of rather poor quality, only displacements of >100 m might have been detectable. Second, the ancient or paleo landslides, being typically characterized by smooth and weathered surface morphologies, partially covered by eolian sand, laharic flows or which have been significantly re-eroded or re-incised by rivers (see also Hermanns et al., 2012).

In order to carry out the recognition and mapping of landslides as much as possible in an orderly and reproducible way, we gridded our study area (cells of 0.5 × 1°) and we explored and mapped analyzing cell by cell. The grid used is provided in the supplementary data. For each identified landslide, a polygon including the headscarp and the slipped mass was drawn (Fig. 5).

3.2. Dimensional and geological landslide parameters

Understanding the occurrence of landslides requires a thorough knowledge of their initial failure conditions. It thus requires data on the terrain morphology (elevation, slope, local relief) on which landslides has developed, on the lithology and on the morphometric characteristics of the landslide itself. For each mapped landslide, we complied this data in a database described in detail below (Supplement, Table 1). This database was further used for statistical analysis of landslides patterns. All calculations were made using ArcGIS software and using the SRTM DEM of 30 m of resolution (SRTM, DOI:/10.5066/F7K072R7). The
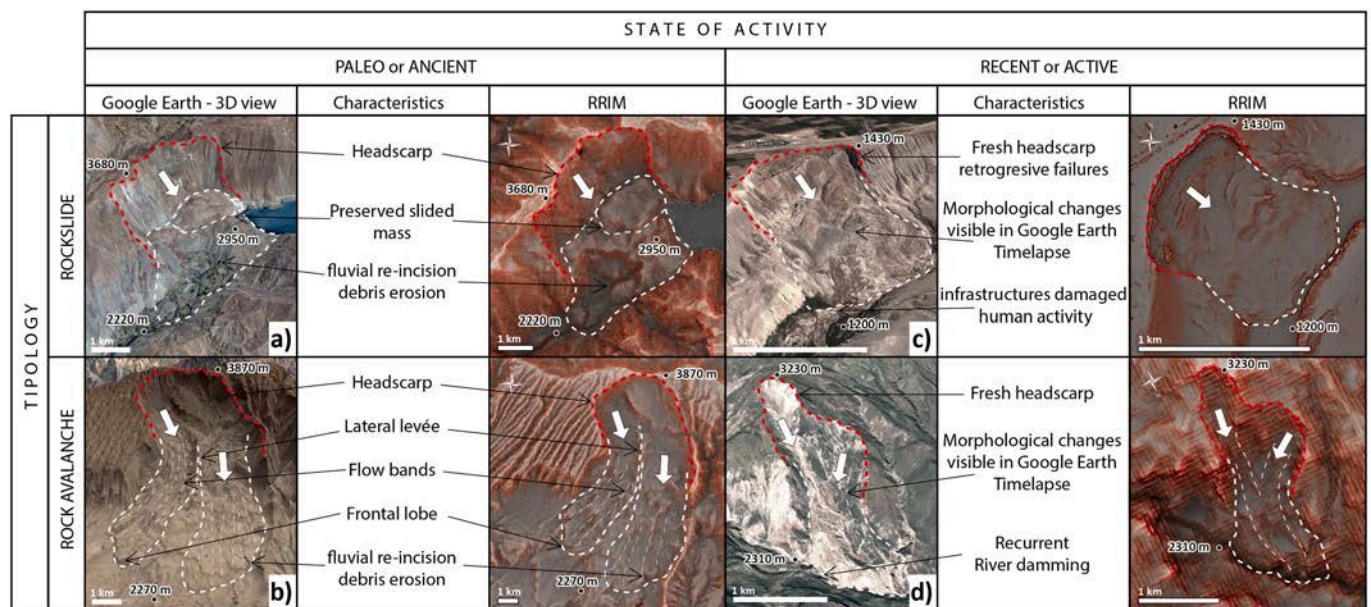

Fig. 4. Morphological criteria used for landslide recognition and mapping along the Central Western Andes. We classified the landslides according to two main typologies (rockslide and rock avalanche) and also attempted to ascribe a qualitative state of activity (paleo or recent) to each identified case (see text for details). Illustrated examples are from (a) the Aricota paleo rockslide (Delgado et al., 2020) (b) the Caquilluco paleo rock avalanche (Zerathe et al., 2017), (c) the Siguas active landslide (Lacroix et al., 2019) and (d) an active landslide from this study (landslide n°109. RRIM: Red Relief Image Map).
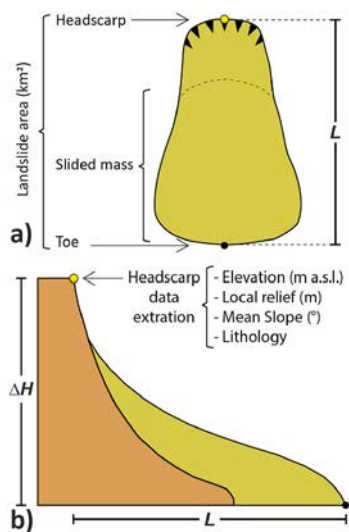
Fig. 5. Landslide sketch illustrating data collection procedure. (a) plan view and b cross-section. The green polygon delimits the whole landslide area (headscarp and slided mass). The yellow dot locates the centroid of the headscarp, considered as the origin of the landslide where several data are extracted (see text for details).

Spatial Analyst tool of ArcGIS toolbox was used to compute slope and local relief map, both calculated considering cells of 2×2 km.

For each landslide, we extracted the area (km²) of the polygon. Then, two points were set: one located at the center of the headscarp and another one located at the landslide toe, in order to indicate the origin of the landslide and its lower limit, respectively (Fig. 5). At the location of the headscarp point, as recommended by Yilmaz and Ercanoglu (2019), we extracted the lithology in which the landslide developed following the lithostratigraphic layers defined in Fig. 2. We also extracted at this location the characteristic of the topography: the elevation (m a.s.l.), the slope (°) and the local relief (m). Finally, using the headscarp point and the toe point, we calculated the landslide length (L in km) and the landslide height (ΔH in km).

All of these morphometric parameters are necessary to perform basic statistical analyses (histograms) of landslide properties in order to better understand their controlling factors. This involves exploring relationships that exist between landslides, topography and lithology through analyzing the frequency distribution of landslides as a function of their area, elevation above sea level, slope and lithology. Through analyzing the relationships ΔH *vs* L and L *vs* A, according to the different landslide type, we also explored the mobility of landslide masses and their dimensional properties.

3.3. Landslide spatial density analysis

The activity of landslides is conditioned by different factors among which are for instance the local relief, the slope, the geology of the site (lithology, faults, structures, etc.). In some areas, the interplay of those factors may generate higher landslide susceptibility and thus landslide clustering. In order to identify if the landslide location responds to a clustering in the western flank of the Central Andes, we applied the Ripley's K Function (Ripley, 1977). This function allows determining statistically if the phenomenon appears to be spatially dispersed, clustered, or randomly distributed throughout the study area. It has been often used to explore the spatial pattern of landslides in previous studies (Tonini et al., 2014; Görum, 2019; Pánek et al., 2019).

Computations were done with the R software (R Core Team, 2019), using the package 'spatstat' (Baddeley et al., 2020). As recommended by Tonini et al. (2014), we applied the "Kinhom" function (Baddeley and Turner, 2005), which is a modification of the original Ripley's

K-function for inhomogeneous point distribution. This variant "Kinhom (r)" allows taking into account the non-stationarity of the studied process due to spatial variability of the geological and topographical characteristics over the studied area (Tonini et al., 2014). The Kinhom(r) function can be defined as (Marcon et Puech, 2009):

$$\widehat{K}_{in\,hom}(r) = \frac{1}{A}\sum_{i=1}^{N}\sum_{j=1, i\neq j}^{N}\frac{c(i,j,r)}{\lambda(i)\lambda(j)} \tag{1}$$

where r is the radius in m, A is the studied area in m², the indicator C (i,j, r) is the average number of neighbors, being equal to 1 if the distance between points i and j equals at most r, or equals 0 otherwise, and λ(i) λ(j) are the process density at points i and j, respectively. Theoretically, when Kinhom(r) = πr^2, the analyzed points are distributed independently (or randomly) from each other. When Kinhom(r) > πr^2, the probability to find a neighboring point at the distance r is greater than the probability to find a point in the same area at any other place, i.e. the points are aggregated. When Kinhom(r) < πr^2, the points are dispersed. Final results were plotted as the Linhom function (Besag and Diggle, 1977), which is a normalization of the Kinhom(r) function to get a benchmark at zero and to facilitate visualization:

$$L(r) = \sqrt{\frac{K(r)}{\pi}} - r \tag{2}$$

We used the centroid of the landslide headscarps (Fig. 5) as point input for the Kinhom analysis as recommended by Yilmaz and Ercanoglu (2019) and references therein. In the case of large destabilized areas (>0.1 km²), with debris that can have long run-out, the landslide headscarp centroids can provide a better assessment of the geological and topographical conditions of the landslide initiation than any other point located along the debris path or at the landslide toe for instance (Yilmaz and Ercanoglu, 2019). Finally, we used the range of radius obtained from this analysis, to calculate a kernel density of landslides over the studied area and to image the point of the higher frequency distribution of landslides.

3.4. Frequency-area relationships

We first explore the distribution of the mapped landslides according to their area using non-cumulated histograms. Then we compute frequency–area distributions (FAD), which is commonly used to explore the statistical properties of landslide inventories, to compare it with sub-datasets of the same region or with other inventories previously published (e.g. Valagussa et al., 2019). Frequency-area distributions are plotted considering landslide-area bins versus their corresponding non-cumulative frequency-density values. It has been defined by Malamud et al. (2004) as:

$$f(A_L) = \delta N_L / \delta A_L \tag{3}$$

where δN_L is the number of landslides with areas between A_L and $A_L + \delta A_L$, A_L being the area of landslide and δA_L is the width of a given landslide area class (bin). The obtained distributions are often plotted in a doubly logarithmic plot (Tebbens, 2020 and references therein). Classically applied to landslides inventoried after strong earthquakes or storms, this analysis revealed that the frequency of landslide-sizes displays a nonlinear pattern through landslide scales (see recent review in Tanyaş et al., 2019). For large to medium landslide ranges, the frequency strongly increases with the decreasing landslide areas, mimicking a negative power-law and suggesting fractal scaling. Then at a certain range of medium landslide area, the frequency area distribution generally shows an inflexion and the power-law no longer applies. Finally, a rollover is sometimes observed for the smallest landslide ranges for which the frequency decreases (Tanyaş et al., 2019).

Two main strategies and derivative interpretations of those distributions exist. Malamud et al. (2004) considered the inflexion and the rollover to represent the natural landslide distribution and proposed a fit

of the complete distribution with a three-parameter inverse gamma distribution. A second strategy (e.g. Pánek et al., 2019; Görum, 2019) is to fit solely the tail of the distribution for medium to large landslides using a power-law above a certain cut-off value of landslide size. For landslide sizes smaller than this cut-off, the inventory is considered as incomplete. Here we applied the second strategy because we chose to map landslides starting from areas of 0.1 km^2 that biases the distribution for small landslide ranges. Moreover, as our inventory stack a large period of time, it is very probable that some of the smallest landslides were eroded.

First, we applied the method of Clauset et al. (2009) focusing on landslide areas only (non-binned). Using the maximum likelihood estimate, it provides the best fit of a power-law, and its exponent labelled alpha, for the landslide-areas higher than a certain cut-off value. To obtain the power-law fit of a frequency-area distribution, the exponent value is converted using the relation beta = alpha +1 (Guzzetti et al., 2002; Clauset et al., 2009). We computed the FAD using equation (3) and applied log-spaced bins that respect two conditions: (1) a low number of bins according to the scale-range of the database and (2) to avoid empty bins.

The power-law exponent generally varies between 1.5 and 3.5 (Tanyaş et al., 2019). It reveals how much large landslides contribute to the inventory. A lower value of β value means a more important contribution of large landslides to the total inventory (Van Den Eeckhaut et al., 2007).

4. Results

4.1. Landslide inventory, typology and morphology

The landslide inventory obtained in this study is presented in Fig. 6 according to the two typologies and state of activity previously defined. The complete landslide database, including all landslide properties and a kmz file of the landslide polygons, are provided in supplementary data. In total, we have identified and mapped more than a thousand landslides distributed between ca. 15 and 20°S along the Western Central Andes, covering a total area of 3782 km^2 (Table 1).

Our results show that gravitational destabilizations along the Western Central Andes are dominated by rockslide typology, representing ~86% of the identified landslides while the rest corresponds to rock avalanche type (Fig. 6a). Importantly, we also show that a great majority of landslides (more than 90%) are paleo landslides. The few active

landslides that we identified are located in specific regions such as the upper Colca valley or the Sihuas region (Fig. 6b).

The landslides distribution over the three main geomorphotectonic units of the western Andean flank is summarized in Table 1. The highest percentage of landslides is found along the Western Cordillera and the Central Depression, each holding 76% and 21% of all the mapped landslides, respectively. Regarding the typologies, the Central Depression is strictly dominated by rockslide type (~99%), while the relative amount of rockslide/rock avalanche type is about 20%/80% for both the Coastal Cordillera and the Western Cordillera. We found that the Western Cordillera and the Central Depression present both about 2% of destabilized areas while the Coastal Cordillera have only 0.3% of its areas affected by large landslides.

4.2. Landslide spatial distributions

Results of the Ripley's K Function applied to our landslide database are plotted on Fig. 7 as the Linhom(r) trend for the whole landslide database (n = 1006), the rockslides (n = 866) and the rock avalanches (n = 140) group. Compared to the theoretical Linhom(r) trend for random data, those results indicate that the landslides are not randomly
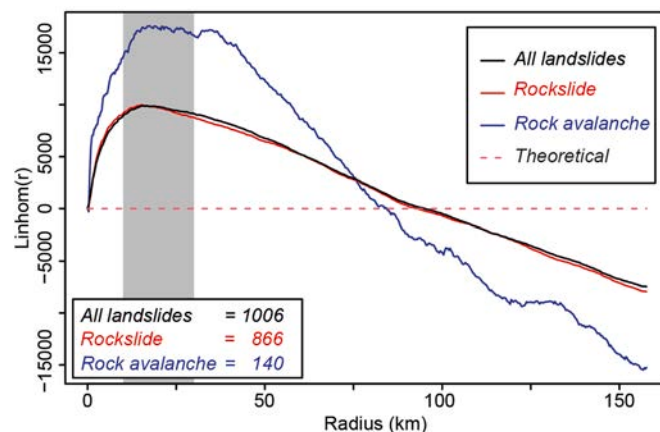

Fig. 7. Results of the Ripley's L-function for our landslide inventory. Grey bar is the range of maximum distribution frequency and is similar for the whole dataset and the two different typologies.
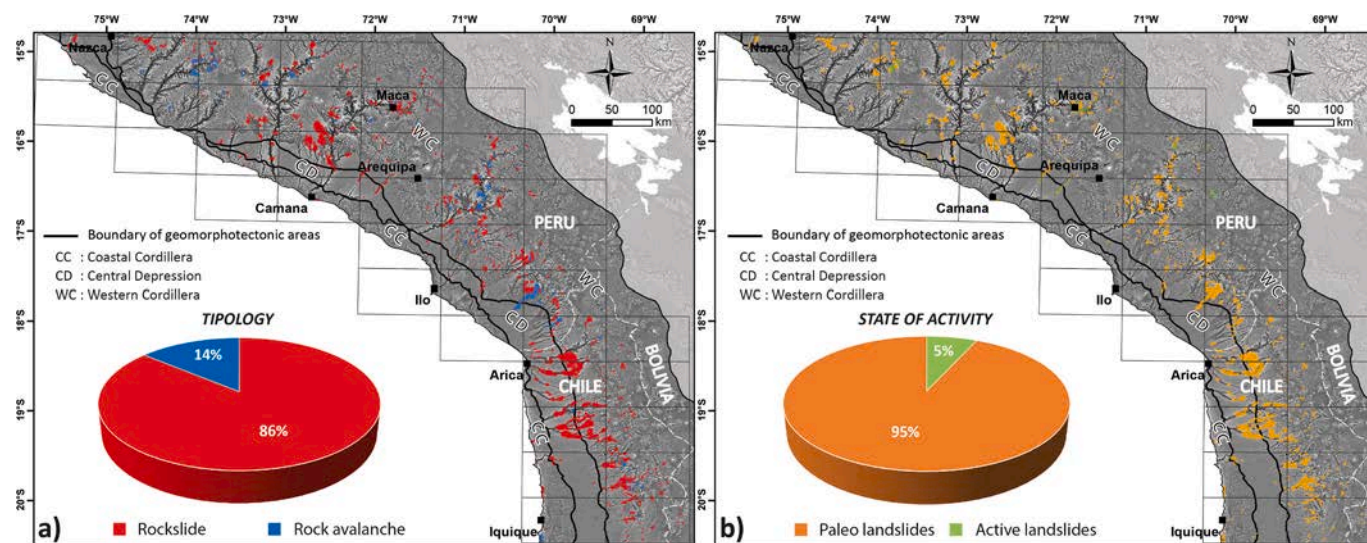

Fig. 6. Landslides inventory along the Western Central Andes between ca. 15 and 20°S. A) Distribution of landslides by typology: rockslide and rock avalanche. B) Landslides distribution according to their state of activity: recent (or active) and paleo. CC: Coastal Cordillera, CD: Central Depression, WC: Western Cordillera. The black grid corresponds to cells of 50 × 100 km that were explored one by one for the landslide mapping (see text for details).

distributed along the western Andean flank, but instead that they display some spatial clustering, with cluster radius up to ca. 100 km. The shape Linhom(r) curves are roughly the same for both the whole dataset and for each individual typology, indicating a similar spatial pattern. The maximum distribution frequency for the different datasets is reached between 10 and 30 km (Fig. 7). This range of radius corresponds to the mean radius of the aggregates of events where the highest number of landslides is found (Goreaud, 2000).

Kernel density maps of landslides were produced using a mean and conservative radius of 20 km (Fig. 8). As expected from the Ripley's K Function analysis, the spatial distribution of large landslides is not homogeneous along the Western Andean flank. Considering the whole landslide database (Fig. 8a), several clusters are revealed, the most significant ones being along the Western Cordillera zone. In particular, we note an important landslide cluster in North Chile at ca. 20°S – 69.5°W between Iquique and Arica latitudes. Three other clusters are located in southernmost Peru, 50 km northeast from Ilo at ca. 17.5°S – 70.5°W, and are aligned along a strike NW-SE. Another cluster is identified 100 km north from Arequipa at ca. 16°S – 71.5°W. This zone corresponds to the upper Colca Valley where numerous landslides have been already reported and studied (e.g. Lacroix et al., 2015). Finally, two smaller clusters are detected at ca.15°S – 74°W and 15°S - 74.5°W, 50 km east from Nazca (Fig. 8a).

The kernel density distribution of rockslide (Fig. 8b) is similar to the one obtained for the whole database (Fig. 8a) consistently with the fact that rockslide is the dominant typology in this inventory. All the clusters previously listed also exist in the rockslide kernel density map (Fig. 8b).

Then, kernel density of rock avalanche also displays also a clustering mainly located along the Western Cordillera (Fig. 8c). The main clusters of rock avalanches coincide with some of the general clusters at ca. 20°S – 69.5°W, ca. 17.5°S – 70.5°W, and ca.15°S – 74°W (Fig. 8c). On the other hand, several other clusters identified for the rockslide type do not appear on the kernel density map of rock avalanches. This suggests some specificities of the factors controlling the rock avalanche processes, that may be different from those controlling rockslide occurrences.

4.3. Landslide size distribution

According to the minimal landslide area considered for this inventory (>0.1 km^2) all the mapped landslides fall in the category "large landslide". The histogram of landslide areas (Fig. 9) shows a strong asymmetrical distribution with a decrease of the number of landslides function to the destabilized surface areas. About 93% of the landslides show areas between 0.1 and 10 km^2 (Fig. 9a). In detail (Fig. 9b), in this range, we still observe this asymmetric trend, the landslide sizes being more represented are the range 0.1–2 km^2, cumulating 67% of landslides. Fig. 9a evidences the absence of landslides for areas ranging between 80 and 170 km^2. Beyond 170 km^2, three giant landslides are recorded (i.e. Chuquibamba, Caquilluco and Lluta). Looking at the cumulative areas, the landslides of the range above 10 km^2 represent more than 50% of the total landslide area although being less represented ($<$7%). The 3 largest landslides are contributing alone to 10% of the total cumulative area. In Fig. 9c, it can be observed that the clusters along the Western Cordillera are dominated by landslides with individual areas smaller than 10 km^2 and located in the headwaters of the main basins and sub-basins. Interestingly, the three largest giant landslides previously mentioned do not belong to the previously described clusters (Fig. 8). Instead, they locate in areas with relatively low to moderate density of landslides. This might suggest that the factors controlling very large landslides are different from those triggering smaller features.

The obtained p-values of the frequency area density distribution of landslides are about ~0.5 (Fig. 10), indicating a good consistency between a power-law model and the tail of our distributions (Clauset et al., 2009). For the whole landslide dataset (ALL), a power-law can be fitted over 2 to 3 orders of magnitude of landslide areas, displaying an
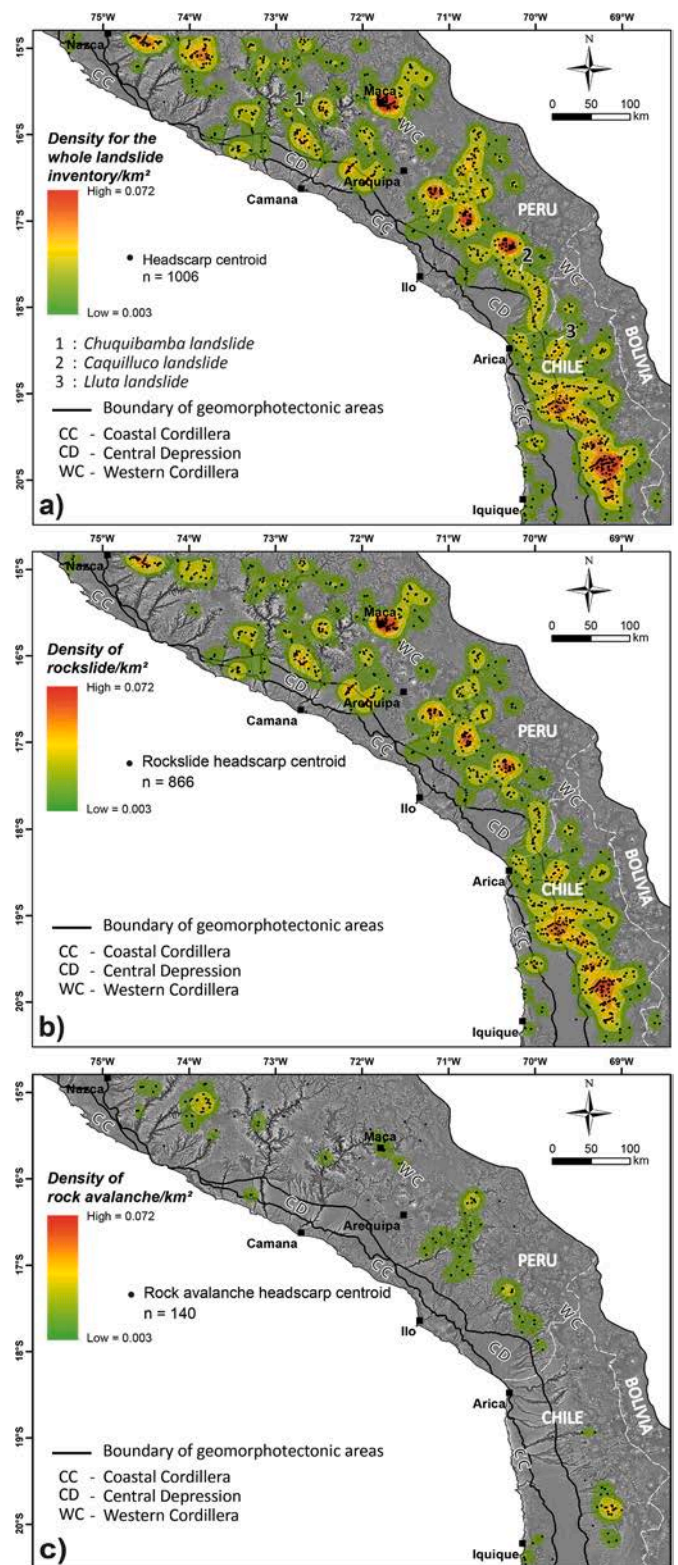

Fig. 8. Spatial distribution analysis of landslides along the western flank of the Central Andes computed thought kernel density analysis using a searching radius 20 km for (a) the whole inventory, (b) the rockslide type and (c) the rock avalanche type.

exponent (beta) of 2.31 ± 0.16 and a cut-off value of $4.0 \pm 1.9 \times 10^6$ m^2. Considering their respective uncertainties, the best-fit parameters of the rockslide and rock avalanche sub datasets remain both almost undifferentiable with those of the whole dataset. We note that the rock
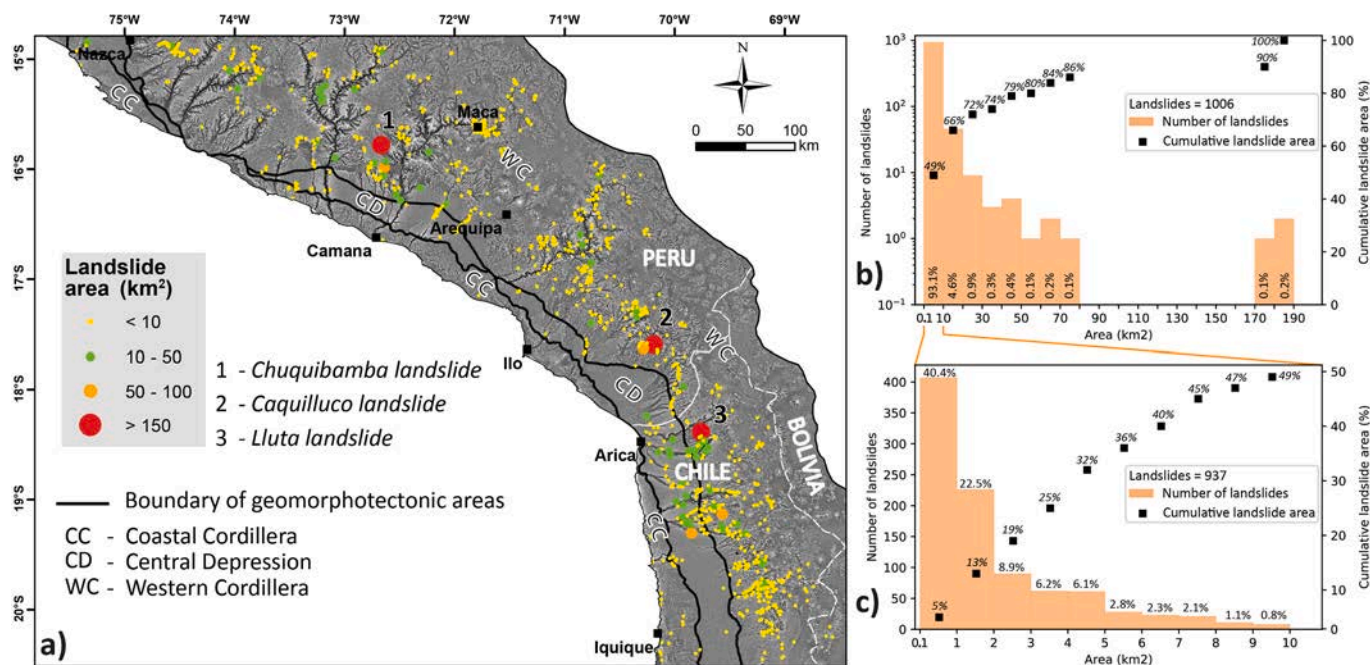
Fig. 9. (a) Spatial distribution of landslides according to their size. Histograms showing the frequency of landslide areas and corresponding cumulative areas in percentage, (b) for the whole dataset using a 10 km^2 bin width and (c) for the sub-range 0.1–10 km^2 using a bin of 1 km^2. CC: Coastal Cordillera, CD: Central Depression, WC: Western Cordillera.
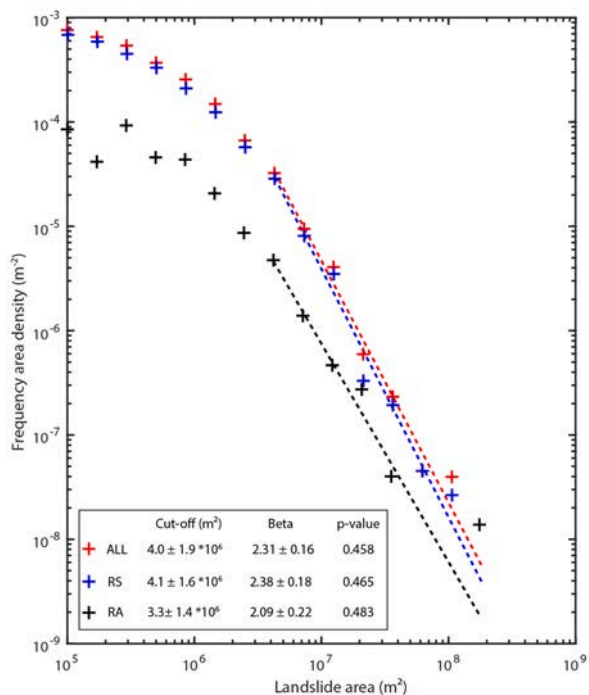

Fig. 10. Frequency area density distributions of landslides in the Central Western Andes given for the whole dataset (ALL) and the sub datasets rockslide (RS) and rock avalanche (RA). The best parameters and associated uncertainties for the power-law fit of the distribution tails are given from the method of Clauset et al. (2009).

avalanche group provides a slight lower power-law exponent (2.09 ± 0.22) which may reflect a dominance of larger landslide features in this typology.

4.4. Landslide morphometry

The analysis of morphometric parameters (ΔH, L and A) associated with the two landslide typologies (rockslide and rock avalanche) provide first order view of the respective landslide dimensions and it highlights some trends (Fig. 11). A correlation (r = ~0.7) is obtained between landslide height (ΔH) versus landslide run-out (L), for both rockslides and rock avalanches, indicating that higher is the landslide height, longer is the run-out of debris (Fig. 11a). The behavior is similar for both typologies as most of the points overlap. The maximum run-out ~41.3 km is obtained for a rock avalanche showing a height of ~3.3 km. However, medians reveal the greater size of rock avalanches, which are about two times higher in length and height than the rockslides (Fig. 11a). A good correlation (r = ~0.9) is also obtained between the landslide run-out (L) and landslide area (A) showing that larger areas are mainly explained by greater landslide lengths (Fig. 11b). Rock avalanches have median areas that are slightly lower than rockslides. Rock avalanches distribution indicates that for the same area than rockslide, rock avalanche debris can reach greater run-out, which is consistent with the highest mobility of granular flows.

5. Interpretation and discussion

5.1. Study limitations

The main limitations of this landslide inventory are the following. 1) Due to the large extension of the study area, it is likely that despite our effort some landslides have been missed during the mapping. We attached a database in. xml format and a file in. kmz format that will serve for future researchers and Peruvian and or Chilean institutions who eventually wish to complete and expand this database. 2) Due to the variability of resolution of the Google Earth images, and sometimes the difficulty leading to the identification of landslide boundaries, we consider that an uncertainty of ca. 100 m applies for the boundary of landslide polygons. This also applies to all the results derived from landslide polygons (landslide area, height, length). 3) In this study, we classified the landslides inventoried into two main categories, rockslide
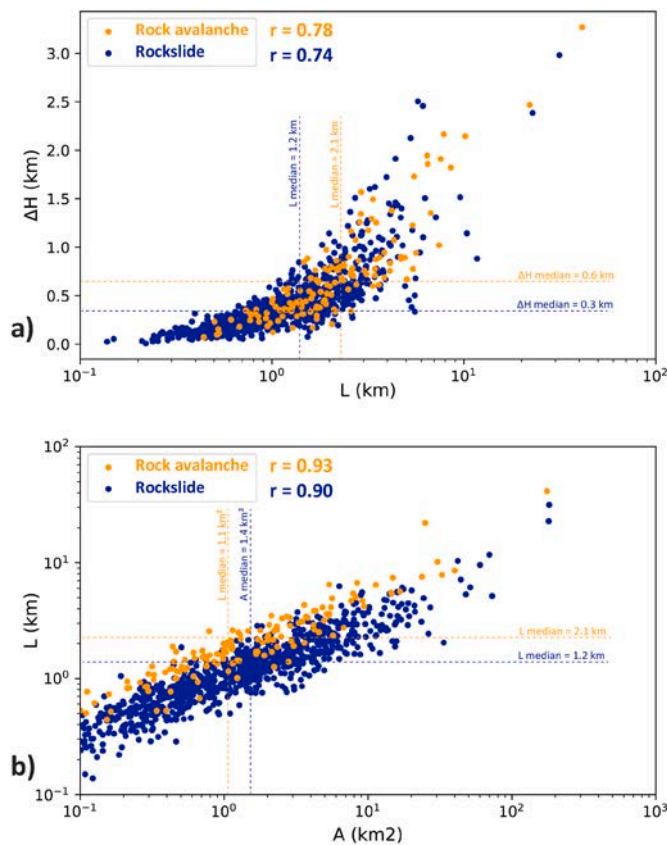
Fig. 11. Morphometric parameters of the landslides for each typology. Relationship between (a) landslide height (ΔH) versus landslide length (L) and (b) landslide length (L) versus landslide area (A). r is the coefficient of correlation of Pearson.

and rock avalanche, as identified by the literature in this region. More details about each landslide feature could be added during future studies, such as to distinguish between planar or rotational failure modes of rockslides to identify their dominant processes. 4) The state of activity of landslides was tentatively defined here according to morphological indices and criteria to differentiate between currently active (or recent) landslides and ancient (or paleo) events. However, the absolute ages of the great majority of the ancient landslides remain unknown and this should be completed with dating methods in future studies. Tracking quantitatively the activity of ongoing landslide failures also would be also very interesting but it requires a dedicated research applying remote sensing methods (e.g. InSAR), applied at a large-scale, which is far beyond the scope of the present study aiming primarily at establishing for the first time a comprehensive inventory of large landslides in the Central Western Andes.

5.2. Landslide controlling factors

In this section we discuss the primary factors that may control or influence landslide susceptibility along the western flank of the Central Andes. We perform comparisons between the landslide frequency distribution and the main settings of this area including the stratigraphy, the relief, the seismotectonic activity and the precipitation patterns.

5.2.1. Landslides versus lithostratigraphy

The type of material (e.g. rock, mud, soil, etc.) is recognized for several decades as one of the first parameters controlling landslide type and their spatial distribution (Varnes, 1978). Several authors further explored the relations between landslides susceptibility and lithology (Hansen, 1984; Guzzetti et al., 1996, 1999; Henriques et al., 2015;

Kumar et al., 2019; Kumar and Gupta, 2021) showing that landslides may vary in typology, dimension and movement rate according to the geomechanical, structural and hydrogeological properties of the material involved (Pradhan and Lee, 2010; Guzzetti et al., 1996). Identifying a specific lithostratigraphic layer prone to landslides can be also useful in terms of hazard management.

Crossing the landslide database with the unified lithostratigraphic map, we explored the relationships between landslides and lithology along the Central Western Andes. In the first order, the results show consistency between the dominant lithologies of the study area and their respective high proportion of landslides (Fig. 12 and Table 2). It concerns mainly: the Quaternary rocks, covering ~27% of the total area and cumulating ~10% of the landslides; the Paleogene-Neogene layers,
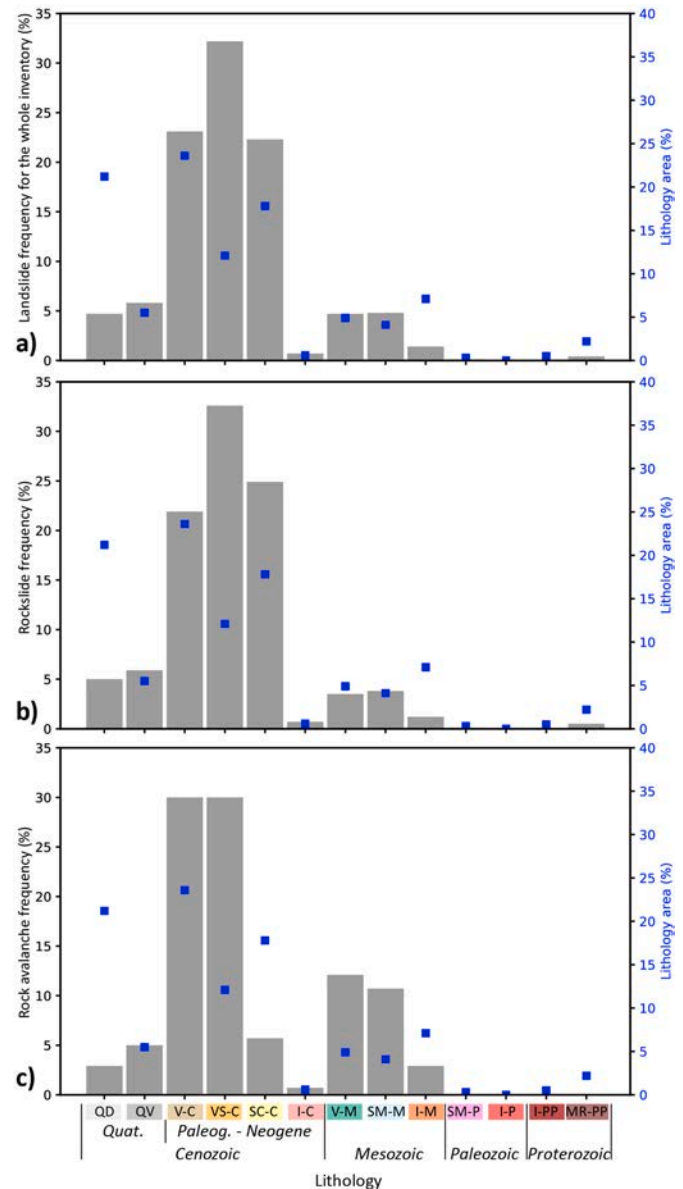

Fig. 12. a) Landslides frequency (in percent) for each lithological unit considering: (a) the whole landslide inventory; (b) the rockslide type and (c) the rock avalanche type. QD: Quaternary deposits (colluvial, fluvial, glacial, eolian); QV: Quaternary volcanic (andesitic lava, volcanic deposits); V–C: Volcanic rock (lava, toba, ignimbrite); SC-C: Sedimentary conglomerate; VS-C: Volcano-Sedimentary (ignimbrite, toba) I–C: Intrusive rocks (granite); V–M: Volcanic rocks (andesite, rhyolite); SM-M: Sediment Marine (limestone and shells); I–M: Intrusive (granite); SM-P: Sedimentary marine; I–P: Intrusive (granite); MR-PP: Metamorphic rocks.

Table 1
Main statistics of the landslide inventory.

Geomorphotectonic areas	Surface of Geomorphotectonic area (km2)	Number of landslides	% of landslides	Type of landslides (Number of landslides = Percentage)	Type of landslides (State of activity = Number of landslides = Percentage)		Total landslide area (km2)	Percentage covered by landslides (% of total area)
					Rockslide (RS)	Rock avalanche (RA)		
Coastal Cordillera (CC)	15620	26	3%	RS (20 = 77%), RA (6 = 23%)	R = 0 = 0%/ P = 20 = 100%	R = 0 = 0%/P = 6 = 100%	52	0.3%
Central Depression (CD)	23198	118	21%	RS (210 = 97%), RA (3 = 3%)	R = 17 = 8%/ P = 193 = 92%)	R = 0 = 0%/P = 3 = 100%	564	2.4%
Western Cordillera (WC)	136033	862	76%	RS (636 = 85%), RA (131 = 15%)	R = 14 = 11%/P = 117 = 89%	R = 14 = 11%/P = 117 = 89%	3166	2.3%
Total	174851	1006	–	–	–	–	3782	2.2%

State of activity: R: Recent or active, P: Paleo.

Table 2
Statistic of landslides versus lithology.

		Lithology Code	Lithostratigraphic	Study area		Landslides statistic					
				Area km^2	%	All landslides	%	Rockslide	%	Rock avalanche	%
Cenozoic	Quaternary	QD	Quaternary Deposits: colluvial, fluvial, glacial, eolian	37036	21.2%	47	4.7%	43	5.0%	4	2.9%
		QV	Quaternary Volcanic: andesitic lava, volcanic deposits	9560	5.5%	58	5.8%	51	5.9%	7	5.0%
			Cumulative	*46596*	*26.7%*	*105*	*10.5%*	*94*	*10.9%*	*11*	*7.9%*
	Paleogene-Neogene	V–C	Volcanic: lava, toba, ignimbrite (Barroso Group)	41126	23.6%	232	23.1%	190	21.9%	42	30.0%
		SC-C	Sedimentary Conglomerate (Moquegua Formation)	30950	17.8%	224	22.3%	216	24.9%	8	5.7%
		VS-C	Volcano-Sedimentary: ignimbrite, toba (Huaylillas formation)	21100	12.1%	324	32.2%	282	32.6%	42	30.0%
		I–C	Intrusive rocks: granite	997	0.6%	7	0.7%	6	0.7%	1	0.7%
			Cumulative	*94173*	*54.1%*	*787*	*78.3%*	*694*	*80.1%*	*93*	*66.4%*
Mesozoic		V-M	Volcanic: andesite, rhyolite (Toquepala formation)	8583	4.9%	47	4.7%	30	3.5%	17	12.1%
		SM-M	Sediment Marine: limestone and shells (Yura Group)	7232	4.1%	48	4.8%	33	3.8%	15	10.7%
		I-M	Intrusive: granite	12350	7.1%	14	1.4%	10	1.2%	4	2.9%
			Cumulative	*28165*	*16.1%*	*109*	*10.9%*	*73*	*8.5%*	*36*	*25.7%*
Paleozoic		SM-P	Sedimentary Marine	576	0.3%	1	0.1%	1	0.1%	–	–
		I–P	Intrusive: granite	10	>0.1%	–	–	–	–	–	–
			Cumulative	*586*	*0.3%*	*1*	*0.1%*	*1*	*0.1%*	*-*	*-*
Proterozoic		I-PP	Intrusive: granite	947	0.5%	–	–	–	–	–	–
		MR-PP	Metamorphic Rocks	3886	2.2%	4	0.4%	4	0.5%	–	–
			Cumulative	*4833*	*2.7%*	*4*	*0.4%*	*4*	*0.5%*		

covering ~54% of the total area and cumulating ~78% of the landslides; the Mesozoic rocks, covering ~16% of the total area, are cumulating ~11% of the landslides. For the Paleogene-Neogene layers (Table 2), that are dominant in the region, we found that ~23% of landslides are located in volcanic rocks (V–C) corresponding to undifferentiated lava; ~20% of landslides located in the Sedimentary conglomerate (SC–C) corresponding to the Moquegua Formation (Fig. 12); ~32% of landslides originated in the volcanic sedimentary rocks (VS–C) corresponding to ignimbrites layers. These results logically indicate that the common occurrence of the different lithology in the study area is roughly representative of the landslide distribution. Nevertheless, a higher general susceptibility for Paleogene-Neogene volcano-sedimentary rocks (VS–C; Huaylillas formation) is shown (Fig. 12a). Those ignimbrites cumulate >30% of the inventoried landslides whereas they only represent ~12% of the study area.

Then some particularities emerge when looking at the landslide type distribution in detail. While the rockslides follow the same pattern as previously described (Fig. 12b), we observe that the rock avalanches are more frequent in the volcanic series (Fig. 12c). The lava, toba and ignimbrite sequences of the Quaternary (QV), Paleogene-Neogene (V–C and VS-C) and Mesozoic (V-M) cumulate more >75% of the rock avalanches (Table 2). This finding can be useful for future studies dedicated to rock avalanche hazard management and call for geotechnical works to better understand why those volcanic sequences are much more prone to rock avalanches. Several previous studies reported, through field observations and data, the strong anisotropy of rock strength of the Paleogene-Neogene volcanic sequences (e.g. García et al., 2004; Strasser and Schlunegger, 2005; Pinto et al., 2008; Irwin et al., 2014) that can be a conditioning factor for landsliding. Indeed, those volcanic sequences are made of weak layers (e.g. unwelded pumice, toba, tuff, volcanic ash, epiclastic layers) alternating with much stronger ones (e.g. lava, pyroclastic flow deposits, ignimbrite) that can have a compressive strength that can be multiple times higher (Irwin et al., 2014). This anisotropy affects also the hydrogeological properties of the material, the weaker layers being much more permeable than the stronger layers (Strasser and Schlunegger, 2005). Three main hypotheses, possibly acting at the

same time, were proposed to explain the slope instabilities in this context: groundwater sapping, flood erosion of strong-over-weak stratigraphy, and the toppling of vertically jointed rock (Irwin et al., 2014).

To the contrary, rock avalanche is almost absent (<5%) from the conglomerates of the Moquegua Formation (Table 2), that is rather affected by rockslides (~25%) (Table 2). This may be due to the fact that this formation has fairly similar overall rock strength, as reported by Graber et al. (2020), in addition to being porous and permeable that can favor the development of listric failure planes and subsequent rockslides

such as the Siguas landslide (Lacroix et al., 2019, 2020).

Finally, we note that the intrusive granite and the metamorphic rocks show particularly low susceptibility to large-scale landslides cumulating only <3% of the total landslide database (Table 2).

5.2.2. Landslides versus relief

In order to explore the link between landslides and relief along the western flank of the Central Andes, we analyzed the relationship between the landslides database and elevation, local relief, mean slope and
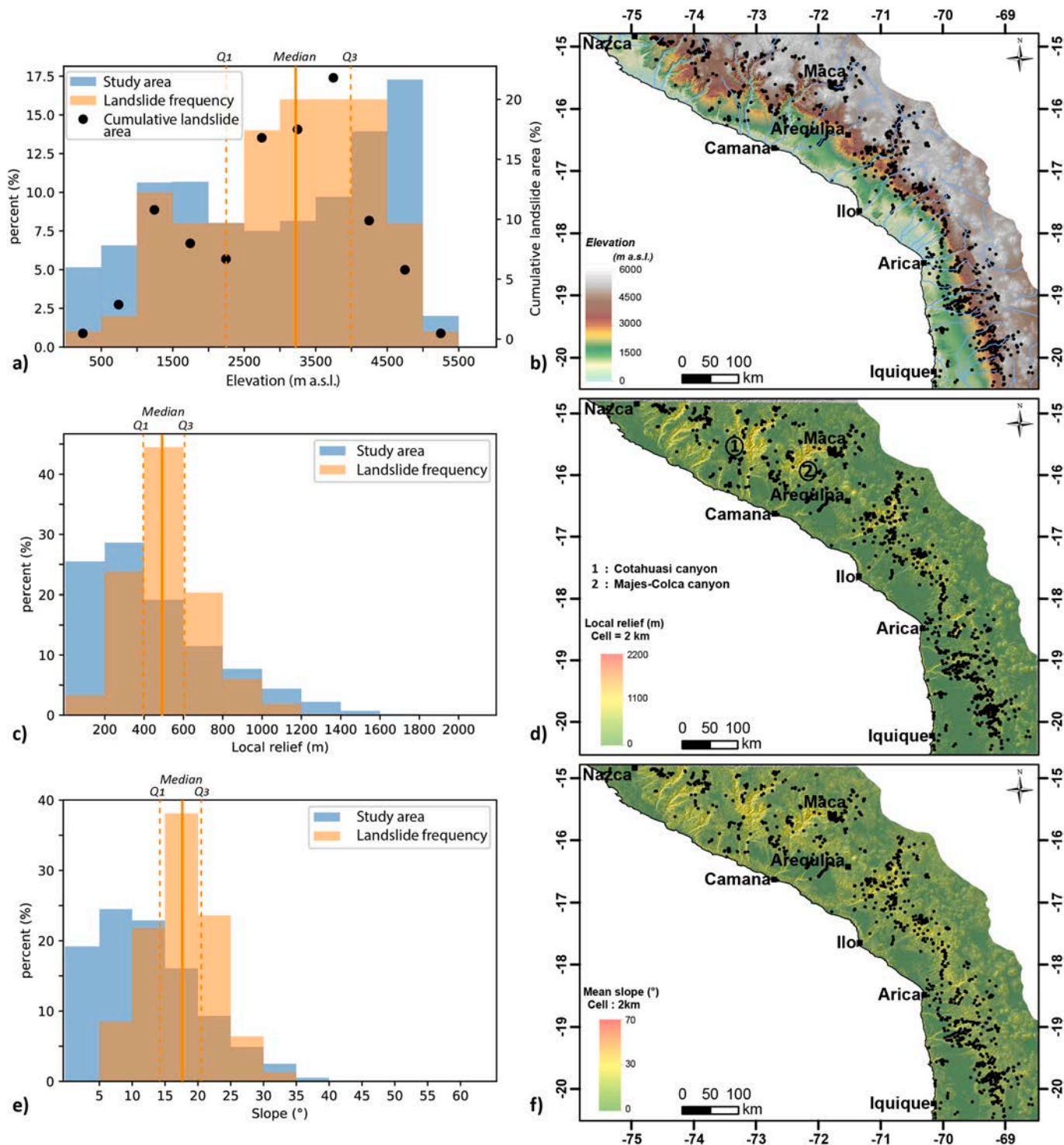

Fig. 13. Landslide statistics versus topography considering (a) and (b) landslide frequency versus elevation, (c) and (d) landslide frequency versus local relief (calculated with cells of 2 × 2 km), (e) and (f) landslide frequency versus slope (calculated with a cell of 2 × 2 km).

river locations. Most of the mapped landslides (~62%) originate in the elevation range between 2500 and 4500 m a.s.l. (Fig. 13a; Fig. 13b) corresponding to the Western Cordillera zone (Fig. 6). Another important range of concentration is between 1000 and 1500 m a.s.l., which corresponds to the Central Depression zone (Fig. 6). Analyzing the cumulative landslide area versus elevation (Fig. 13a; Fig. 13b), we found that >50% of the cumulative landslide areas are between 2500 and 4000 m. a.s.l. (Fig. 13a). This means that landslides are both more frequent and larger in this range of elevation, thus contributing more to the erosion budget. The higher landslide frequency in this elevation range may also be explained by a co-correlation with the lithology of the Western Cordillera unit, that is dominated by volcanic Paleogene-Neogene rocks, that are highly prone to destabilizations as we have previously seen (Fig. 12).

The comparison between landslides and local relief show a unimodal distribution (Fig. 12c). Very few landslides (<5%) are recorded below 200 m of local relief (Fig. 13c). More than 90% of the landslides originate between the local relief ranging from 200 to 800 m (Fig. 13c; Fig. 13d), with the highest frequency peak between 400 and 600 m corresponding to ~50% of the landslides (quartiles Q1 and Q3, Fig. 13c). Then, the frequency of landslides is lower for the greater local relief, <10% of landslides being located in range 800–1000 m. Finally, almost no landslide (<1%) are recorded for the highest local relief ranging from 1000 to 1600 m, despite that they are sharing ~8% of the total study area (Fig. 13c). Those strong reliefs (1000–1600 m) mainly correspond to the deepest and central parts of the Cotahuasi and Majes-Colca canyons, that are almost landslide-free (Fig. 13d). Looking at the mean slope of the study area, the general pattern of landslides distribution previously described is similar, ~80% of the landslides occurring between the range of 10° and 25°, with 50% of those originating on slopes between 14 and 21° (Q1 and Q3 respectively). From slopes >30°, the occurrence of landslides is minimal (<2%).

Those results slightly differ from what is commonly reported from others large landslides inventories, where an asymmetric landslide frequency versus relief (or slope) is often obtained: the highest landslide frequency being concentrated in the highest local relief (e.g. Görum, 2019; Pánek et al., 2019; Junquera-Torrado et al., 2019). The worldwide compilation of large landslides provided by Korup et al. (2007) also shows this tendency, half of giant landslides occurring in the steepest 15% of mountainous terrain. The higher frequency of landslides in the steepest relief has been related to the threshold hillslope concept (Korup et al., 2007), predicting that above a certain hillslope-angle, or local relief, mountain flanks may fail readily because of the limitation of landscape-scale rock strength (e.g. Schmidt and Montgomery, 1995; Larsen and Montgomery, 2012; Roering, 2012).

In our study area, we interpret the almost absence of large landslides in the areas of extreme relief (1000–1600 m) as due to a lithological effect. Indeed, the deepest sections of the Cotahuasi and Majes-Colca canyons are incised through strong lithologies such as intrusive granite, metamorphic rocks and/or limestone (Fig. 2). Those lithologies having great strength, it is probable that those canyon incisions could reach such depth without occurrence of large to very large landslides. The valley flank erosion in those contexts might be dominated by debris flows, scree, which mobilize smaller volumes of rock that are not documented in this inventory. On the other hand, looking at the general spatial distribution of large landslides at the scale of the study area (Fig. 3d) and excepting the cases the central Cotahuasi and Majes-Colca canyons, we note that the landslides distribution mainly follows the river network and their incisions, where most of the local relief locates (Fig. 3c and d). This suggests that the lithological control on large landslide susceptibility might dominate, whereas the relief would come as secondary.

5.2.3. Landslides versus seismicity and active faults

The link between landslide and seismicity has been well documented by the literature in the Central Western Andes, either for earthquake-induced landslides activity (e.g. Keefer and Moseley, 2004; Lacroix et al., 2013; Lacroix et al., 2015) or to tentatively link paleo landslide records with the seismogenic context of the Andes (e.g. Mc Philips et al., 2014; Crosta et al., 2017; Junquera-;Torrado et al., 2021). In Fig. 14, we confront the landslide density from this study to the seismicity recorded and the main active faults. To what concern the seismicity related to the subduction, there is no evidence of an increase of landslide density closer to the subduction (Fig. 14). This may be explained by the fact that landslides eventually triggered by subduction earthquakes remain relatively small (e.g. Lacroix et al., 2013). Indeed, the inventory from Lacroix et al. (2013) indicates that the ~866 landslides were triggered during the Pisco mega-earthquake (Mw8.0) were (1) relatively small, with areas ranging between 10^{-4} to 10^{-1} km^2; and (2) they mostly corresponded to rockfalls and superficial topples along roads. To explain the fact that a rather low number of landslides were triggered by this Mw8.0 earthquake, while around 10^5 triggered landslides would be predicted for such magnitude (Keefer, 2002), the authors evoked (1) the attenuation of the waves due to the depth of the seismic source and its distance with the relief (>80 km), (2) the climate setting of the region, which long term aridity does not favor soil development and strongly limits the bedrock weathering and the groundwater saturation. Observations were similar for the other historical or recent mega earthquakes of subduction such as the Arequipa Mw8.4 (2001) in southern Peru or the Iquique Mw8.1 (2014) in northern Chile (Fig. 14), for which no observation of triggering, nor reactivation of large landslides (>1 km^2) were ever reported (see Borrero 2002; Stirling et al., 2002; Candia et al., 2017). At the plurimillenial-scale, Mc Phillips et al. (2014) suggest a link between landslide triggering and subduction earthquakes in the Pisco region but again it concerns relatively small landslide sizes from 10^{-3} to 10^{-1} km^2. Those different examples strongly contrast with our mapping showing a thousand of large to giant landslides (areas up to 180 km^2) that are well-preserved along the arid Central Western Andes. In summary, given the previous statements, we suggest that while the subduction seismicity can indeed trigger small to moderate superficial landslides and rockfalls, it probably plays a negligible role in forcing large-scale and deep-seated landslides in the arid conditions of the Western Cordillera. On the other hand, frequent and recurrent subduction earthquakes (Mw8 has a recurrence of 100–300 yrs; Chlieh et al., 2011) can contribute to the long-term weathering and rock damage as reported by Keefer and Moseley (2004) observing pervasive coseismic ground cracking and microfracturing of hillslope during the 2001 Arequipa earthquake.

The other source of seismicity along the Central Western Andes is produced by crustal faults activity. In Fig. 14, we confront the landslide density to the neotectonic fault network as well as to the crustal seismicity. As previously stated (δ2.4), no crustal shallow earthquake of Mw > 6 occurred in this region during the last fifty years. One exception is the region of Maca (Fig. 14) where a seismic swarm (Mw~5) clearly correlates with a landslide cluster. In this region landslides are very specific, developing in lacustrine sediments of a paleolake (Zerathe et al., 2016), where several studies (Lacroix et al., 2015; Lacroix et al., 2019; Bontemps et al., 2018; Gaidzik et al., 2020) already pointed the effect of frequent local earthquakes linked to the volcanic activity.

Another interesting point is the well-marked spatial correlation at large-scale between the landslide clusters and the neotectonics fault pattern (Fig. 14). This correlation can be observed (1) in Peru where several landslides clusters are aligned, from Arequipa to Tacna, with the Incapuquio Fault System (IFS); and (2) in Chile where the West-Vergent Thrust System (WTS) overlaps the main landslide clusters (Fig. 14). Several interpretations can be raised. First, those faults play an important role in the relief building (e.g. Hall et al., 2008), thus the landslide-fault correlation might be indirect, these landslide clusters being rather linked to the relief. Second, those faults are associated with thick damage zones of kilometer width, where the rock strength is decreased and the deep-water circulation along fractures is enhanced. Third, there might be a link between paleoseismicity and paleo landslide
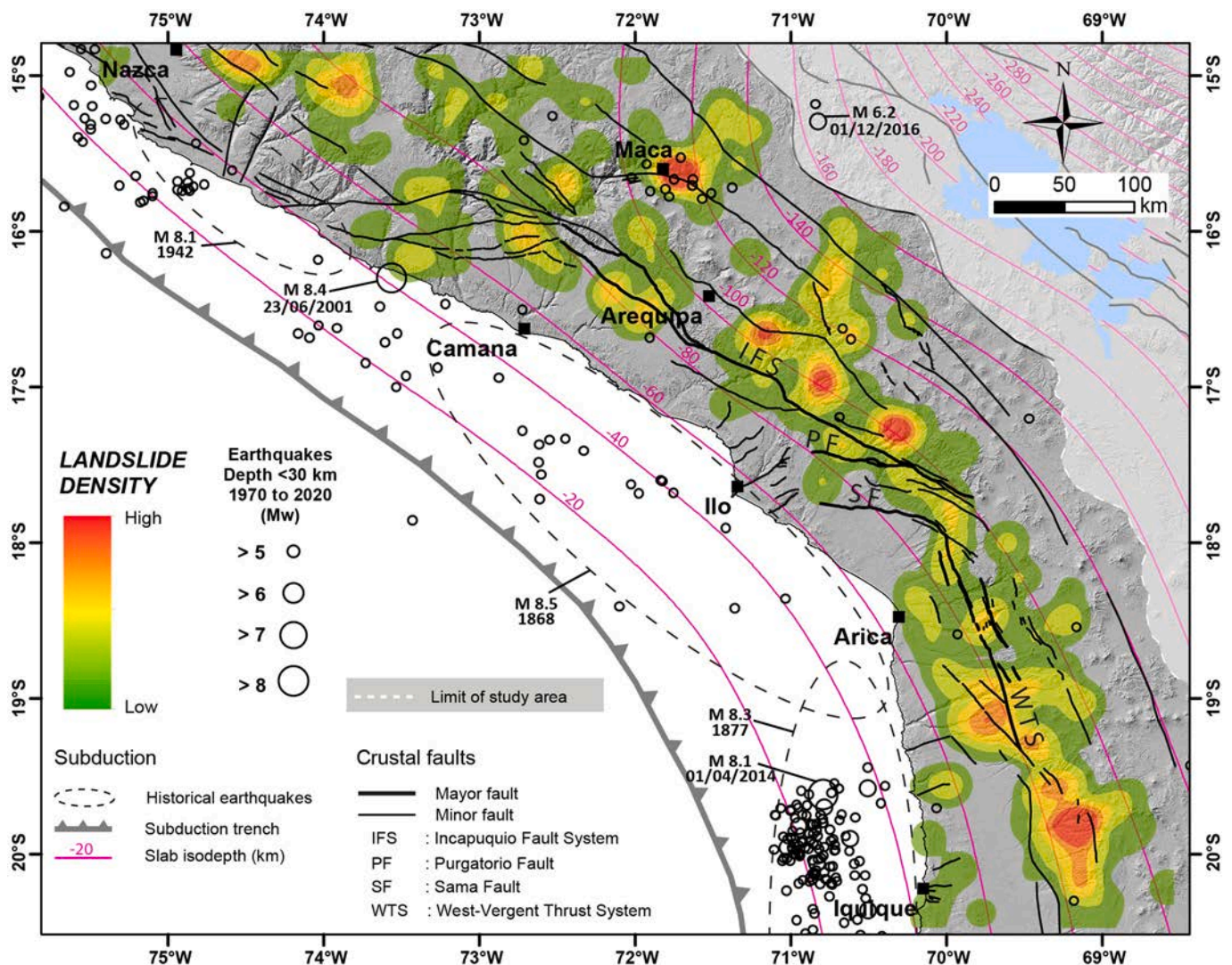
Fig. 14. Landslides density (from Fig. 8a) along the Central Western Andes confronted to the instrumental seismic catalogues for the last 50 years from USGS (earthquakes >Mw5 and depth <30 km), the available historical seismicity and to the main neotectonics crustal faults (see references on the caption of Fig. 3).

triggering. This discussion is speculative because the timing of paleo-earthquakes and paleo landslides remain largely undocumented. However, Benavente et al. (2017b) revealed that tectonic activity occurred along the Purgatorio fault in the last thousand years, showing two ruptures of ~3 and ~2 m of vertical surface offset, equivalent to seismic events of ~Mw7. Evidence of tectonic activities have been also revealed along the ~400 km long IFS (Benavente et al., 2021), where paleo-seismic trenching shows at least 2–3 m of net slip in the last 500 years interpreted as single Mw7.4–7.7 earthquake. Basically, the susceptibility that a bedrock landslide could be triggered or reactivated by an earthquake (Fan et al., 2019) depends on several parameters: (1) the local rock mass properties (linked to the lithology, frequency of fractures and joint discontinuities, etc.) and the level of hillslope stability, and (2) the local ground motion produced by the earthquake that is modulated by the distance from the source and local site effect of wave amplification (topography, lithological contrast, etc.). For crustal earthquakes, relationships between landslide size and ground motion, with larger and deeper landslides associated with higher ground motion, have been reported (Valagussa et al., 2019). Case studies of earthquake-induced landslides inventories after an event of Mw7 and beyond showed that the larger landslides (>0.1 km^2) are found generally in areas where the peak ground acceleration exceed 0.5 g, in the close field of the fault (at 10–20 km of the fault) (Valagussa et al., 2019; Junquera-Torrado et al.,

2021). Therefore, it is likely that some of the inventoried large landslides in the western central Andes near the major IFS and WTS faults were triggered by past earthquakes along these faults. There is a need for more research carried out on the timing of both crustal faults and paleo landslides in this part of the Andes.

5.2.4. Landslides versus rainfall

Rainfall is the most frequent forcing and triggering factor of mass movements in mountainous areas. Physical processes related to the addition of water on or below the earth's surface and their effects on slope instabilities are well described by hydro-mechanical models (e.g., critical soil-state mechanics and rate-and-state friction) developed from numerical theory (Iverson et al., 2000; Baum et al., 2010) coupled to laboratory experiments and confronted to in-situ landslide monitoring and statistics (Glade et al., 2000; Dai and Lee, 2001). The influence of rainfall on landslides differs substantially upon landslide type (typology, dimension, depth), the material involved (mechanical and hydrological properties) and the characteristic of the rainfall (intensity and duration). Groundwater recharge acts as a key factor for slope failures by decreasing the resistance of materials due to pore water pressure variations (Iverson et al., 2000). While shallow landslides (1–2 m depth) are usually triggered a few hours or days after the rainfall onset, depending on the time required for water infiltration and critical pore pressure

increase (Iverson et al., 2000; Baum et al., 2010), larger and deeper landslides (depth >10 m), which are the case of study in this inventory, are more likely to respond to a much longer rainfall duration (months to years). Deep-seated landslides are often in subcritical stability state and subject to long term creep deformation (Lacroix and Amitrano, 2013). These slow movements progressively increase the rock damage and the permeability, reducing the whole landslide strength, until the strain localizes along basal shear failure surfaces (Eberhardt et al., 2004) and a catastrophic collapse can ultimately occur. As shown by recent studies (Handwerger et al., 2019; Agliardi et al., 2020), the conditions for the collapse triggering are often: (1) the presence of a long-term water table water-saturating the basal shear zone; and (2) short-term pore-pressure increase linked to rapid water recharges.

Active landslides are mainly located in the northern part of the study area, where the mean annual rainfall is the highest (Fig. 15a). About 70% of the active landslides are found in areas receiving more than 400 mm/year of rainfall (Fig. 15b). This is consistent with the threshold of 500 mm/yr that have been previously documented for the triggering of the Colca landslides (Zerathe et al., 2016; Bontemps et al., 2018). On the other hand, no active landslides were identified in the desertic south-western part of the study area (Fig. 15). One exception is a group of active anthropic landslides located ~50 km west of Arequipa (Fig. 15; Lacroix et al., 2020; Graber et al., 2021) which develop along the flanks of the Siguas and the Vitor valleys (Fig. 16). They correspond actually to paleo landslides that have been re-activated for ~40 years due to irrigation water input for agricultural lands located just uphill the destabilized valley flanks (Hermann et al., 2012; Araujo et al., 2017; Lacroix et al., 2020). Recently, Graber et al. (2021) demonstrated the critical role played by the anthropic groundwater table rise for those landslide reactivations. Moreover, several other large ancient landslides of the same type are located on the opposite valley flanks and they remain inactive in the absence of irrigation on those sides (Fig. 16). This suggests that the past activation of those ancient landslides could have been linked to climatic conditions that were not the same as nowadays, much more humid, allowing local rainfall and long-term natural recharge of the water table.

At large-scale over the whole study area, the distribution of paleo landslides is not consistent with the current rainfall pattern. They display an inverse relation with rainfall, drier being the region, higher being the paleo landslide frequency (Fig. 15c). About 70% of the paleo landslides are located in areas that currently receive less than 300 mm/yr of rainfall (Fig. 15c). This distribution might be explained by the fact that drier conditions favor long-term preservation of the paleo-landslide forms. If more humid, younger failures and erosion would have erased those relics. However, considering the hydro-mechanical conditions required for the triggering of deep-seated landslides, it is on the other hand very improbable that those collapses occurred in such arid conditions. As shown with many examples in the literature (Odin et al., 2018) and the cases of Siguas-Vitor valleys (Graber et al., 2021), the triggering of those large landslides requires a significant recharge of water tables, that are only allowed by perennial rainfall over several months to years. Despite producing very strong storms, the intense rainfalls linked to only few days long El Niño events are very unlikely to feed such groundwater recharge. The rock-hard ground and the lack of vegetation does not allow water absorption and only lead to surficial erosion and flashfloods (Aguilar et al., 2020). On the other hand, ongoing researches on paleoclimate reconstructions in the region show that the Atacama Desert and the Central Western Andes could have experienced more long-term (years to millennial) climate variability during the Pleistocene, as recorded in alluvial fan progradation (Ritter et al., 2019, 2020), paleolake development (Ritter et al., 2019), alluvial terraces sequences (Steffen et al., 2010) and groundwater discharge deposits (Saez et al., 2016). The few giant paleo landslides that were dated have failure ages that are consistent with those events (e.g. Aricota rockslide, ~18 ka with Henrich Stadial (Delgado et al., 2020); the Chuquibamba (~100 ka) and the Caquilluco rock avalanches (100–120 ka) with the Ouki event (Margirier et al., 2015; Zerathe et al., 2017). It is probable that such persistent humid periods have produced sufficient aquifer recharge promoting the triggering of those large landslides. More dating of landslides coupled with local paleo climatic studies are required to disentangle those questions.

6. Conclusion

We report in this paper an original inventory of large landslides (>0.1 km^2) along the hyper arid Central Western Andes (latitudes ca.
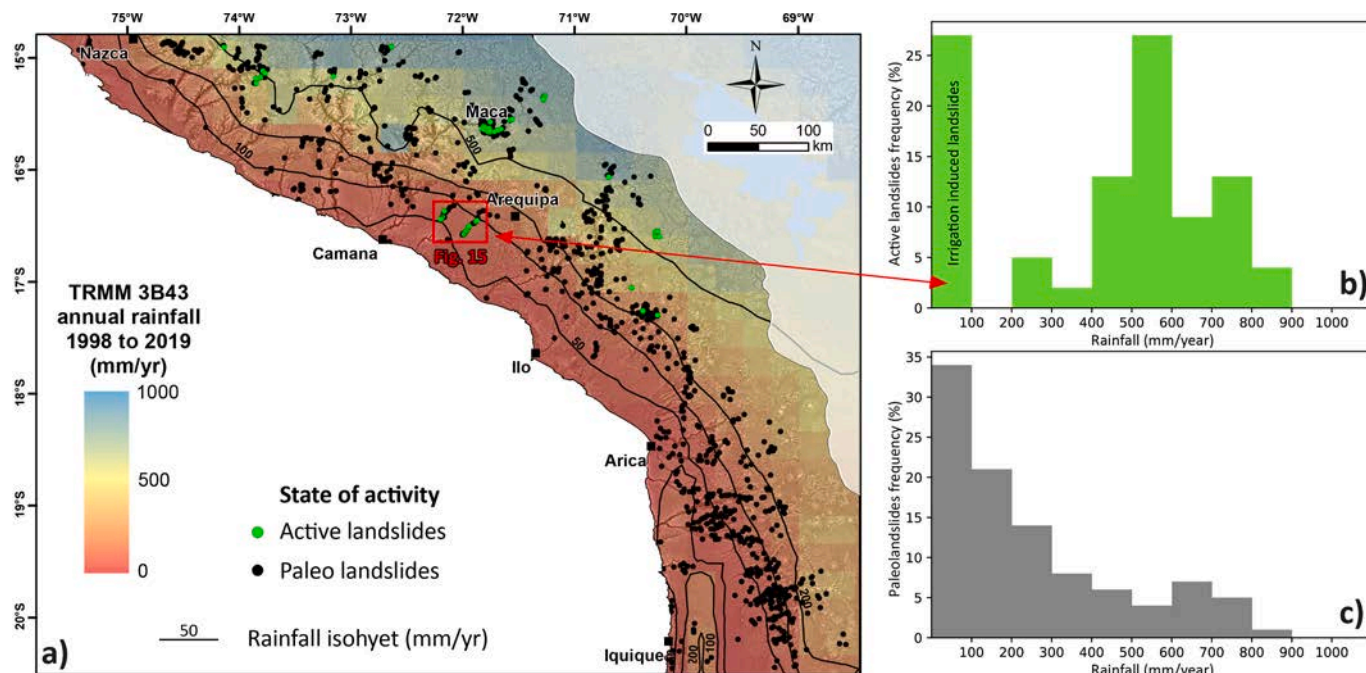

Fig. 15. a) Landslide inventory along the Central Western Andes compared to the mean rainfall of the last two decades; b) and c) Frequency of recent and ancient landslides, respectively, versus rainfall patterns.
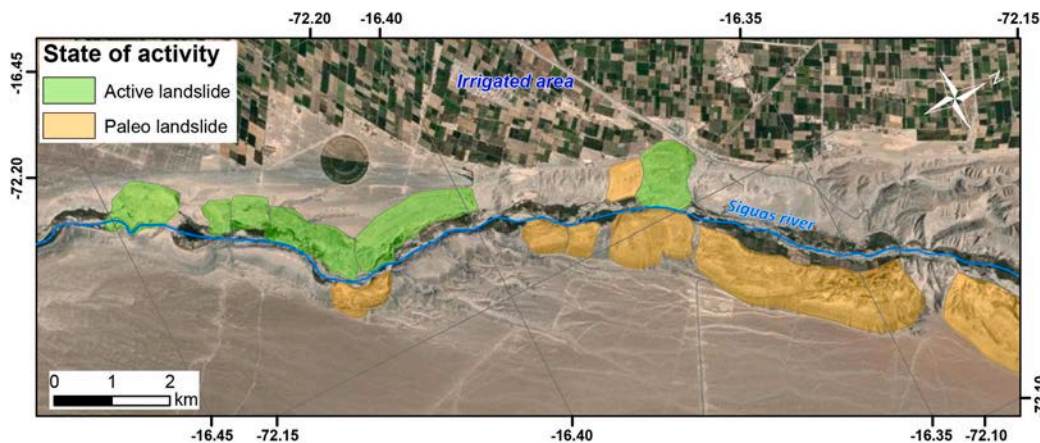
Fig. 16. Anthropic reactivation of paleo landslides induced by irrigation for agriculture along (a) the Siguas valley modified from Graber et al. (2021). See location on Fig. 13. a. The Identification of the landslides reactivated by irrigation comes from Lacroix et al. (2020) while the location of the paleo landslides is from this study. Of importance is the fact that the re-activation of those paleo landslides has need more than 40 years of constant irrigation to increase sufficiently the groundwater level, suggesting that a very different climate must have been acting there at past to produce similar conditions.

15° to 20°S). A systematic mapping of newly identified landslides by satellite images, Google Earth and DEMs analysis, added to the compilation of previous works, allows the inventory of more than a thousand large slope failures. The destabilized area covers ~3782 km^2 and represents about 2% of the whole study area. Landslide size distribution follows a power-law with an exponent of 2.31 ± 0.16 and a cut-off of 4.0 ± 1.9 km^2, the largest landslides being up to 180 km^2 in size. According to the landslide typologies, the rockslides (or coherent landslides) are the dominant failure mode representing 86% of the inventory while the rock avalanches (granular landslides) represent 14%. The statistical analysis of this landslide inventory confronted to topographical, geological constraints of this region provides first-order understanding about the main conditioning factors of slope failures in the Central Western Andes. We identified a combination of a lithological and relief effects on landslide distribution. Ignimbrites of the Paleogene-Neogene (Hualylillas Formation) concentrate about 30% of the inventoried landslides. The majority of landslides has developed along the flanks of valleys incising thought the Western Cordillera. Nevertheless, the deepest areas of two major canyons (Majes-Colca and Cotahuasi) appear less prone to large landslide failure, possibly because they are incising through granite. Finally, we identified a control of fracturing and weathering related to the long-term fault activity suggested by the spatial correlation between landslide clustering and the regional crustal faults network.

This new landslide inventory provides perspectives on the respective roles of climatic and seismotectonic forcing's on the landslide activity in the Central Western Andes. Our dataset suggests that subduction seismicity play a negligible role in forcing those large landslides, while the clustered landslide distribution suggests a more efficient role of crustal seismicity. The majority of the mapped landslides corresponds to paleo landslides (more than 90%), mainly located in the driest areas (rainfall <300 mm/yr). On the other hand, the sole active landslides either anthropic, controlled by water infiltration due to irrigation, or either located in the northern part of the study area receiving rainfall from the Amazonian monsoon (>400 mm/year). We suggest that the triggering of those paleo landslides could not have been possible in the dry conditions of the Central Western Andes, even during strong earthquakes. Alternatively, the period of activity of those paleo landslides may have been related to long-term (years to millennial) climate shift toward more humid conditions during the Pleistocene, and possibly coupled to seismic effect. Next challenging researches will be to add chronological constraints on this landslide inventory to explore possible temporal correlations between periods of landslide activity and external seismic and/or climatic cycles.

CRediT authorship contribution statement

Fabrizio Delgado: Writing – original draft, Methodology,

Investigation, Formal analysis, Conceptualization. **Swann Zerathe:** Writing – review & editing, Validation, Supervision, Project administration, Methodology, Investigation, Funding acquisition, Formal analysis, Conceptualization. **Stéphane Schwartz:** Writing – review & editing, Validation, Supervision, Project administration, Investigation, Funding acquisition. **Bastien Mathieux:** Investigation, Formal analysis. **Carlos Benavente:** Supervision, Project administration.

Declaration of competing interest

Acknowledgments

Appendix A. Supplementary data

Supplementary data associated with this article can be found, in the online version, at https://doi.org/10.1016/j.jsames.2022.103824.

References

Acosta, H., Alván, A., Mamani, M., Oviedo, M., Rodríguez, J., 2011. Mapa Geológico del cuadrángulo de La Yarada (37-u), Hoja 37-u-IV. Dirección de Geología Regional (INGEMMET), Lima, Perú. Serie (A), 1 mapa.

Allmendinger, R.W., Jordan, T.E., Kay, S.M., Isacks, B.L., 1997. The evolution of the Altiplano puna of the central Andes. Annu. Rev. Earth Planet Sci. 25, 139–174.

Armijo, R., Lacassin, R., Coudurier-Curveur, A., Carrizo, D., 2015. Coupled tectonic evolution of Andean orogeny and global climate. Earth Sci. Rev. 143, 1–35.

Audin, L., Bechir, A., 2006. Active tectonics as determinant factor in landslides along the western cordillera? Presented at the congreso peruano de Geologia, 13, Lima. Resumenes extendidos, Sociedad Geológica del Perú xxii, 237–239. October 17–20.

Audin, L., Hérail, G., Riquelme, R., Darrozes, J., Martinod, J., Font, E., 2003. Geomorphological markers of faulting and neotectonic activity along the western Andean margin, northern Chile. J. Quat. Sci. 18 (8), 681–694.

Audin, L., David, C., Hall, S., Farber, D., Hérail, G., 2006. Geomorphic evidences of recent tectonic activity in the forearc, southern Peru. Rev. Asoc. Geol. Argent. 61 (4), 545–554.

Audin, L., Lacan, P., Tavera, H., Bondoux, F., 2008. Upper plate deformation and seismic barrier in front of Nazca subduction zone: the Chololo Fault System and active tectonics along the Coastal Cordillera, southern Peru. Tectonophysics 459, 174–185.

Baddeley, A., Turner, R., 2005. spatstat: an R package for analyzing spatial point patterns. J. Stat. Software 12 (6), 1–42.

Baddeley, A.D., Hitch, G.J., Allen, R.J., 2020. A Multicomponent Model of Working Memory. Oxford University Press, Oxford.

Barrientos, S., Vera, E., Alvarado, P., Monfret, T., 2004. Crustal seismicity in Central Chile. J. South Am. Earth Sci. 16, 759–768.

Bellido, E., 1979. Geología del cuadrángulo de Moquegua. INGEMMET, Boletín, Serie A: Carta Geológica Nacional 15, 78.

Bellido Bravo, E., Guevara, C., 1963. Geología de los cuadrángulos de Punta de Bonbon y Clemesí. Com. Carta Geol. Nacional., Lima bol. no 5.

Bellon, H., Lefevre, Cl, 1916. Données géochronometriques sur le volcanisme andin dans le Sud du Pérou. Implications géochrono-tectoniques. C. R. Acad. Sci. 283, 1–4.

Benavente, C., Audin, L., 2009. Geometría, morfología y peligro sísmico de la falla Purgatorio Mirave - antearco del sur del Perú. Bol. Soc. Geol. Peru 103 (15), 15–26.

Benavente, C., Delgado, G., García, B., Aguirre, E., Audin, L., 2017a. Neotectónica, evolución del relieve y peligro sísmico en la región Arequipa. INGEMMET, Boletín Serie C: Geodin. Ing. Geol. 64, 370.

Benavente, C., Zerathe, S., Audin, L., Hall, S., Robert, X., Delgado, F., Farber, D.L., ASTER Team., 2017b. Active compressional tectonics in the Andean forearc of southern Peru evidenced by direct 10Be surface exposure dating of an active fault scarp. Tectonics 36 (9), 1662–1678.

Benavente, C., Rosell, L., García, B., Palomino, A., Aguirre, E., Taipe, E., Robert, X., 2021. Neotectónica de la región Tacna. INGEMMET, Boletín, Serie C: Geodin. Ing. Geol. 84, 171 pp., 1 mapa.

Besag, J., Diggle, P.J., 1977. Simple Monte Carlo tests for spatial pattern. J. Roy. Stat. Soc. C-App. 26, 327–333.

Blanco, N., Tomlinson, A., 2013. Carta Guatacondo, Región de Tarapacá. Servicio Nacional de Geología y Minería, Carta Geológica de Chile. Serie Geología Básica 156, 1 mapa escala 1:100.000. Santiago.

Bontemps, N., Lacroix, P., Doin, M.P., 2018. Inversion of deformation fields time-series from optical images, and application to the long term kinematics of slow-moving landslides in Peru. Rem. Sens. Environ. 210, 144–158.

Candia, G., De Pascale, G.P., Montalva, G., Ledezma, C., 2017. Geotechnical aspects of the 2015 Mw 8.3 Illapel megathrust earthquake sequence in Chile. Earthq. Spectra 33 (2), 709–728.

Casquet, C., Fanning, C.M., Galindo, C., Pankhurst, R.J., Rapela, C.W., Torres, P., 2010. The Arequipa massif of Peru: new SHRIMP and isotope constraints on a paleoproterozoic inlier in the grenvillian orogen. J. S. Am. Earth Sci. 29 (1), 128–142.

Chlieh, M., Perfettini, H., Tavera, H., Avouac, J.P., Remy, D., Nocquet, J.M., Rolandone, F., Bondoux, F., Gabalda, G., Bonvalot, S., 2011. Interseismic coupling and seismic potential along the Central Andes subduction zone. J. Geophys. Res. Solid Earth 116 (B12). https://doi.org/10.1029/2010JB008166.

Clauset, A., Shalizi, C.R., Newman, M.E., 2009. Power-law distributions in empirical data. SIAM Rev. 51, 661–703.

Cobbing, E.J., Pitcher, W.S., 1972. The coastal batholith of central Peru. J. Geol. Soc. 128 (5), 421–454.

Cobbing, E.J., Ozard, J.M., Snelling, N.J., 1977. Reconnaissance geochronology of the crystalline basement rocks of the Coastal Cordillera of southern Peru. Geol. Soc. Am. Bull. 88 (2), 241–246.

Crosta, G.B., Hermanns, R.L., Frattini, P., Valbuzzi, E., Valagussa, A., 2014. Large slope instabilities in northern Chile: inventory, characterisation and possible triggers. In: Proceedings of the 3rd World Landslide Forum, 2–6 June 2014, p. 6. https://doi.org/10.1007/978/-3-319-04996-0_28. Bejing.

Crosta, G.B., Paolo, F., Elena, V., Hermanns, R.L., 2015. The Cerro Caquilluco–Cerrillos Negros Giant Rock Avalanches (Tacna, Peru). IAEG, p. N159. Torino 2014.

Crosta, G.B., Hermanns, R.L., Dehls, J., Lari, S., Sepulveda, S., 2017. Rock avalanches clusters along the northern Chile coastal scarp. Geomorphology 289, 27–43.

Delgado, F., Zerathe, S., Audin, L., Schwartz, S., Benavente, C., Carcaillet, J., Bourles, D. L., ASTER Team, 2020. Giant landslide triggerings and paleoprecipitations in the Central Western Andes: the aricota rockslide dam (South Peru). Geomorphology 350. https://doi.org/10.1016/j.geomorph.2019.106932.

Dorbath, L., Cisternas, A., Dorbath, C., 1990. Assessment of the size of large and great historical earthquakes in Peru. Bull. Seismol. Soc. Am. 80 (3), 551–576.

Dunai, T.J., Gonzalez López, G.A., Juez-Larré, J., 2005. Oligocene–Miocene age ofaridity in the Atacama desert revealed by exposure dating of erosion-sensitivelandforms. Geology 33 (4), 321–324.

Eberhardt, E., Stead, D., Coggan, J.S., 2004. Numerical analysis of initiation and progressive failure in natural rock slopes—the 1991 Randa rockslide. Int. J. Rock Mech. Min. Sci. 41, 69–87. https://doi.org/10.1016/S1365-1609(03)00076-5.

Evenstar, L.A., Mather, A.E., Hartley, A.J., Stuart, F.M., Sparks, R.S.J., Cooper, F.J., 2017. Geomorphology on geologic timescales: evolution of the late cenozoic pacific paleosurface in northern Chile and southern Peru. Earth Sci. Rev. 171, 1–27.

Farías, M., Charrier, R., Comte, D., Martinod, J., Hérail, G., 2005. Late Cenozoic deformation and uplift of the western flank of the Altiplano: evidence from the depositional, tectonic, and geomorphologic evolution and shallow seismic activity (northern Chile at 19°30`S). Tectonics 24, 1–27.

Froude, M.J., Petley, D.N., 2018. Global fatal landslide occurrence from 2004 to 2016. Nat. Hazards Earth Syst. Sci. 18 (8), 2161–2181.

Gaidzik, K., Żaba, J., Ciesielczuk, J., 2020. Tectonic control on slow-moving andean landslides in the Colca valley, Peru. J. Mt. Sci. 17 (8), 1807–1825.

García, M., Gardeweg, M., Clavero, J., Hérail, G., 2004. Hoja Arica, Región de Tarapacá. Servicio Nacional de Geología y Minería, Carta Geológica de Chile. Serie Geología Básica 84, 150, 1 mapa escala 1:250.000.

García, M., Fuentes, G., Riquelme, F., 2013. Carta Miñimiñi, Regiones de Arica y Parinacota y de Tarapacá. Servicio Nacional de Geología y Minería, Carta Geológica de Chile. Serie Geología Básica 157, 49 pp., 1 mapa escala 1:100.000.

Gariano, S.L., Guzzetti, F., 2016. Landslides in a changing climate. Earth Sci. Rev. 162, 227–252.

Garzione, C.N., Hoke, G.D., Libarkin, J.C., Withers, S., MacFadden, B., Eiler, J., Ghosh, P., Mulch, A., 2008. Rise of the Andes. Science 320, 1304–1307.

Gayo, E.M., Latorre, C., Jordan, T.E., Nester, P.L., Estay, S.A., Ojeda, K.F., Santoro, C.M., 2012. Late Quaternary hydrological and ecological changes in the hyperarid core of the northern Atacama Desert (~ 21 S). Earth Sci. Rev. 113 (3–4), 120–140.

González, G., Salazar, P., Loveless, J.P., Allmendinger, R.W., Aron, F., Shrivastava, M., 2015. Upper plate reverse fault reactivation and the unclamping of the megathrust during the 2014 northern Chile earthquake sequence. Geology 43 (8), 671–674.

Goreaud, F., 2000. Apports de l'analyse de la structure spatiale en forêt tempérée à l'étude et la modélisation des peuplements complexes. Ph.D. thesis. Ecole Nationale du Génie Rural, des Eaux et des Forêts, France.

Görum, T., 2019. Tectonic, topographic and rock-type influences on large landslides at the northern margin of the Anatolian Plateau. Landslides 16, 333–346.

Gunnell, Y., Thouret, J.C., Brichau, S., Carter, A., Gallagher, K., 2010. Low-temperature thermochronology in the Peruvian Central Andes: implications for long-term continental denudation, timing of plateau uplift, canyon incision and lithosphere dynamics. J. Geol. Soc. 167 (4), 803–815.

Guzzetti, F., Cardinali, M., Reichenbach, P., 1996. The influence of structural setting and lithology on landslide type and pattern. Environ. Eng. Geosci. 2 (4), 531–555.

Guzzetti, F., Carrara, A., Cardinali, M., Reichenbach, P., 1999. Landslide hazard evaluation: a review of current techniques and their application in a multi-scale study, Central Italy. Geomorphology 31 (1–4), 181–216.

Guzzetti, F., Malamud, B.D., Turcotte, D.L., Reichenbach, P., 2002. Power-law correlations of landslide areas in central Italy. Earth Planet Sci. Lett. 195, 169–183.

Guzzetti, F., Mondini, A.C., Cardinali, M., Fiorucci, F., Santangelo, M., Chang, K.T., 2012. Landslide inventory maps: new tools for an old problem. Earth Sci. Rev. 112, 42–66.

Hall, S.R., Farber, D.L., Audin, L., Finkel, R.C., Mériaux, A.S., 2008. Geochronology of pediment surfaces in southern Peru: implications for Quaternary deformation of the Andean forearc. Tectonophysics 459 (1), 186–205. https://doi.org/10.1016/j.tecto.2007.11.073.

Hansen, A., 1984. Engineering geomorphology: the application of an evolutionary model of Hong Kong`s terrain. Z. Geomorphol. 51, 39–50.

Haque, U., Da Silva, P.F., Devoli, G., Pilz, J., Zhao, B., Khaloua, A., Glass, G.E., 2019. The human cost of global warming: deadly landslides and their triggers (1995–2014). Sci. Total Environ. 682, 673–684.

Hartley, A.J., Chong, G., 2002. Late pliocene age for the Atacama Desert: implications for the desertification of western south America. Geology 30 (1), 43–46.

Haschke, M., Günther, A., Melnick, D., Echtler, H., Reutter, K.J., Scheuber, E., Oncken, O., 2006. Central and southern Andean tectonic evolution inferred from arc magmatism. In: The Andes. Springer, Berlin, Heidelberg, pp. 337–353.

Henriques, C., Zêzere, J.L., Marques, F., 2015. The role of the lithological setting on the landslide pattern and distribution. Eng. Geol. 189, 17–31.

Houston, J., Hartley, A.J., 2003. The Central Andean west-slope rainshadow and its potential contribution to the origin of hyper-aridity in the Atacama Desert. Int. J. Climatol. 23, 1453–1464.

Irwin III, R.P., Tooth, S., Craddock, R.A., Howard, A.D., de Latour, A.B., 2014. Origin and development of theater-headed valleys in the Atacama Desert, northern Chile: morphological analogs to martian valley networks. Icarus 243, 296–310.

Isacks, B.L., 1988. Uplift of the central Andean plateau and bending of the Bolivian orocline. J. Geophys. Res. 93, 3211–3231.

Jacay, J., Sempere, T., Husson, L., Pino, A., 2002. Structural characteristics of the Incapuquio fault system, southern Peru. In: V International Symposium on Andean Geodynamics ISAG, Extended Abstracts, pp. 319–321. Toulouse, France.

James, D.E., Sacks, I.S., 1999. Cenozoic formation of the Central Andes: a geophysical perspective. In: Skinner, B.J. (Ed.), Geology and Ore Deposits of the Central Andes, vol. 7. Society of Economic Geologists, Special Publication, pp. 1–25.

Junquera-Torrado, S., Moreiras, S.M., Sepúlveda, S.A., 2019. Distribution of landslides along the Andean active orogenic front (Argentinean Precordillera 31–33° S). Quat. Int. 512, 18–34.

Junquera-Torrado, S., Moreiras, S.M., Rodriguez-Peces, M.J., Sepulveda, S.A., 2021. Linking earthquake-triggered paleolandslides to their seismic source and to the possible seismic event that originated them in a portion of the Argentine Precordillera (31°–33°S). Nat. Hazards 106, 43–78. https://doi.org/10.1007/s11069-020-04447-1.

Keefer, D.K., 2002. Investigating landslides caused by earthquakes–a historical review. Surv. Geophys. 23 (6), 473–510.

Keefer, D.K., Moseley, M.E., 2004. Southern Peru desert shattered by the great 2001 earthquake: implications for paleoseismic and paleo-El Niño–Southern Oscillation records. Proc. Natl. Acad. Sci. Unit. States Am. 101 (30), 10878–10883.

Keefer, D.K., Moseley, M.E., DeFrance, S.D., 2003. A 38 000-year record of floods and debris flows in the Ilo region of southern Peru and its relation to El Niño events and great earthquakes. Palaeogeogr. Palaeoclimatol. Palaeoecol. 194 (1–3), 41–77.

Kelleher, J.A., 1972. Rupture zones of large South American earthquakes and some predictions. J. Geophys. Res. 77 (11), 2087–2103.

Korup, O., Clague, J.J., Hermanns, R.L., Hewitt, K., Strom, A.L., Weidinger, J.T., 2007. Giant landslides topography and erosion. Earth Planet Sci. Lett. 261, 578–589.

Kumar, S., Gupta, V., 2021. Evaluation of spatial probability of landslides using bivariate and multivariate approaches in the Goriganga valley, Kumaun Himalaya, India. Nat. Hazards 1–28.

Kumar, V., Gupta, V., Jamir, I., Chattoraj, S.L., 2019. Evaluation of potential landslide damming: case study of Urni landslide, Kinnaur, Satluj valley, India. Geosci. Front. 10 (2), 753–767.

Lacroix, P., Amitrano, D., 2013. Long-term dynamics of rockslides and damage propagation inferred from mechanical modeling. J. Geophys. Res.: Earth Surf. 118 (4), 2292–2307.

Lacroix, P., Zavala, B., Berthier, E., Audin, L., 2013. Supervised method of landslide inventory using panchromatic SPOT5 images and application to the earthquake-triggered landslides of Pisco (Peru, 2007, Mw8. 0). Rem. Sens. 5 (6), 2590–2616.

Lacroix, P., Berthier, E., Taipe, E., 2015. Earthquake-driven acceleration of slow-moving landslides in the Colca valley, Peru, detected from Pléiades images. Rem. Sens. Environ. 165, 148–158. https://doi.org/10.1016/j.rse.2015.05.010.

Lacroix, P., Araujo, G., Hollingsworth, J., Taipe, E., 2019. Self-entrainment motion of a slow-moving landslide inferred from landsat-8 time series. J. Geophys. Res.: Earth Surf. 124 (5), 1201–1216.

Lacroix, P., Dehecq, A., Taipe, E., 2020. Irrigation-triggered landslides in a Peruvian desert caused by modern intensive farming. Nat. Geosci. 13 (1), 56–60.

Larsen, I.J., Montgomery, D.R., 2012. Landslide erosion coupled to tectonics and river incision. Nat. Geosci. 5 (7), 468–473.

Lavenu, A., 2005. Fallas Cuaternarias de Chile, vol. 62. Servicio Nacional de Geología y Minería, Boletín, Santiago, p. 71.

Lavenu, A., Thiele, R., Machette, M., Dart, R., Bradley, L., Haller, K., 2000. Maps and Database of Quaternary Faults in Bolivia and Chile, p. 50. U.S. Geological Survey Open-File Report 00-283.

Leyton, F., Ruiz, S., Sepúlveda, S., 2010. Reevaluación del peligro sísmico probabilístico en Chile Central. Andean Geol. 37 (2), 455–472. https://doi.org/10.5027/andgeoV37n2-a11.

Litty, C., Duller, R., Schlunegger, F., 2016. Paleohydraulic reconstruction of a 40 ka-old terrace sequence implies that water discharge was larger than today. Earth Surf. Process. Landforms 41 (7), 884–898.

Malamud, B.D., Turcotte, D.L., Guzzetti, F., Reichenbach, P., 2004. Landslides, earthquakes, and erosion. Earth Planet Sci. Lett. 229 (1–2), 45–59.

Mamani, M., Tassara, A., Wörner, G., 2008. Composition and structural control of crustal domains in the central Andes. G-cubed 9 (3). https://doi.org/10.1029/2007GC001925.

Mamani, M., Wörner, G., Sempere, T., 2009. Geochemical variations in igneous rocks of the Central Andean Orocline (13° to 18°S): tracing crustal thickening and magma generation through time and space. Geol. Soc. Am. Bull. 122, 162–182. https://doi.org/10.1130/B26538.1.

Mamani, M., Navarro, P., Carlotto, V., Acosta, H., Rodriguez, J., Jaimes, F., Santos, A., Rodríguez, R., Chavez, L., Cueva, E., Cereceda, C., 2010. Arcos magmáticos meso-cenozoicos del Perú. In: XV Congreso Peruano de Geología, Cusco. Sociedad Geológica del Perú, Resúmenes Extendidos, pp. 563–566.

Mamani, M., Rodriguez, R., Acosta, H., Jaimes, F., Navarro, P., Carlotto, V., 2012. Caracteristicas litológicas y geoquímicas más resaltantes de los arcos magmáticos del Peru desde el Ordovicico. XVI Congreso Peruano de Geologia, p. 5 resúmenes extendidos.

Marc, O., Stumpf, A., Malet, J.P., Gosset, M., Uchida, T., Chiang, S.H., 2018. Towards a global database of rainfall-induced landslide inventories: first insights from past and new events. Earth Surf. Dyn. Discuss. https://doi.org/10.5194/esurf-2018-20.

Margirier, A., Audin, L., Carcaillet, J., Schwartz, S., 2015. Tectonic and climatic controls on the Chuquibamba landslide (western Andes, southern Peru). Earth Surf. Dynam. Discuss. 2, 1129–1153.

Mariño, J., Samaniego, P., Manrique, N., Valderrama, P., Roche, O., de Vries, B.V.W., Liorzou, C., 2021. The Tutupaca volcanic complex (Southern Peru): eruptive chronology and successive destabilization of a dacitic dome complex. J. S. Am. Earth Sci. 109, 103227.

Martinod, J., Gérault, M., Husson, L., Regard, V., 2020. Widening of the Andes: an interplay between subduction dynamics and crustal wedge tectonics. Earth Sci. Rev. 204, 103170.

Mather, A.E., Hartley, A.J., Griffiths, J.S., 2014. The giant coastal landslides of Northern Chile: tectonic and climate interactions on a classic convergent plate margin. Earth Planet Sci. Lett. 388, 249–256.

Medwedeff, W.G., Clark, M.K., Zekkos, D., West, A.J., 2020. Characteristic landslide distributions: an investigation of landscape controls on landslide size. Earth Planet Sci. Lett. 539, 116203.

Monge, R., Cervantes, J., 2000. Memoria explicativa de la geología del cuadrángulo de Pachía (36v) y Palca (36x). Dirección de Geología Regional del INGEMMET, Lima, Perú, p. 11.

Montgomery, D.R., 2001. Slope distributions, threshold hillslopes, and steady-state topography. Am. J. Sci. 301 (4–5), 432–454.

Morandé, J., Gallardo, F., Farías, M., 2015. Carta Guaviña, Región de Tarapacá. Servicio Nacional de Geología y Minería, Carta Geológica de Chile. Serie Geología Básica 177, 1 mapa escala 1:100.000.

Mukasa, S.B., Henry, D.J., 1990. The San Nicolas batholith of coastal Peru: early Palaeozoic continental arc or continental rift magmatism? J. Geol. Soc. 147 (1), 27–39.

New, M., Lister, D., Hulme, M., Makin, I., 2002. A high-resolution data set of surface climate over global land areas. Clim. Res. 21 (1), 1–25.

Newell, N.D., 1945. Investigaciones geológicas en las zonas circunvecinas al lago Titicaca. Boletín Sociedad Geológica del Perú 18, 44–68.

Pánek, T., 2019. Landslides and Quaternary climate changes—the state of the art. Earth Sci. Rev. 196, 102871.

Pánek, T., Břežný, M., Kapustová, V., Lenart, J., Chalupa, V., 2019. Large landslides and deep-seated gravitational slope deformations in the Czech Flysch Carpathians: new LiDAR-based inventory. Geomorphology 346, 106852.

Pardo-Casas, F., Molnar, P., 1987. Relative motion of the Nazca (farallon) and south-American plates since late cretaceous time. Tectonics 6, 233–248.

Petley, D., 2012. Global patterns of loss of life from landslides. Geology 40 (10), 927–930.

Pinto, L., Hérail, G., Charrier, R., 2004. Sedimentación sintectónica asociada a las estructuras Neógenas en la Precordillera de la zona de Moquella (19°15'S, norte de Chile). Rev. Geol. Chile 31 (1), 19–44. https://doi.org/10.5027/andgeoV31n1-a02.

Pinto, L., Hérail, G., Fontan, F., de Parseval, P., 2007. Neogene erosion and uplift of the western edge of the Andean Plateau as determined by detrital heavy mineral analysis. Sediment. Geol. 195, 217–237.

Pinto, L., Hérail, G., Sepúlveda, S.A., Krop, P., 2008. A Neogene giant landslide in Tarapacá, northern Chile: a signal of instability of the westernmost Altiplano and palaeoseismicity effects. Geomorphology 102 (3–4), 532–541.

Placzek, C.J., Quade, J., Patchett, P.J., 2013. A 130 ka reconstruction of rainfall on the Bolivian Altiplano. Earth Planet Sci. Lett. 363, 97–108.

Pradhan, B., Lee, S., 2010. Landslide susceptibility assessment and factor effect analysis: backpropagation artificial neural networks and their comparison with frequency ratio and bivariate logistic regression modelling. Environ. Model. Software 25 (6), 747–759.

Proyecto Multinacional Andino, P.M.A.(, 2009. Geociencia para las Comunidades Andinas. Atlas de deformaciones cuaternarias de los Andes. Servicio Nacional de Geología y Minería, Publicación Geológica Multinacional 7, 320 pp., 1 mapa en CD. Santiago.

Quade, J., Rech, J.A., Betancourt, J.L., Latorre, C., Quade, B., Rylander, K.A., Fisher, T., 2008. Paleowetlands and regional climate change in the central Atacama Desert, northern Chile. Quat. Res. 69 (3), 343–360.

Quang, C.X., Clark, A.H., Lee, J.K., Hawkes, N., 2005. Response of supergene processes to episodic Cenozoic uplift, pediment erosion, and ignimbrite eruption in the porphyry copper province of southern Peru. Econ. Geol. 100 (1), 87–114.

R Core Team, 2019. R: A Language and Environment for Statistical Computing. R Foundation for Statistical Computing, Vienna, Austria. https://www.R-project.org/.

Ripley, B.D., 1977. Modelling spatial patterns. J. Roy. Stat. Soc. B 39 (2), 172–212.

Ritter, B., Binnie, S.A., Stuart, F.M., Wennrich, V., Dunai, T.J., 2018. Evidence for multiple Plio-Pleistocene lake episodes in the hyperarid Atacama Desert. Quat. Geochronol. 44, 1–12.

Ritter, B., Wennrich, V., Medialdea, A., Brill, D., King, G., Schneiderwind, S., Niemann, K., Fernández-Galego, E., Diederich, J., Rolf, C., Bao, R., Melles, M., Dunai, T.J., 2019. Climatic fluctuations in the hyperarid core of the Atacama Desert during the past 215 ka. Sci. Rep. 9 (1), 1–13.

Rivera, M., Samaniego, P., Vela, J., Le Pennec, J.L., Guillou, H., Paquette, J.L., Liorzou, C., 2020. The eruptive chronology of the Yucamane-Calientes compound volcano: a potentially active edifice of the Central Andes (southern Peru). J. Volcanol. Geoth. Res. 393, 106787.

Roering, J., 2012. Landslides limit mountain relief. Nat. Geosci. 5 (7), 446–447.

Roperch, P., Sempere, T., Macedo, O., Arriagada, C., Fornari, M., Tapia, C., García, M., Laj, C., 2006. Counterclockwise rotation of late Eocene-Oligocene fore-arc deposits in southern Perú and its significance for oroclinal bending in the central Andes. Tectonics 25 (3), 1–29. https://doi.org/10.1029/2005TC001882.

Salinas, E., 1985. Evolución paleogeográfica del Sur del Perú a la luz de los métodos de análisis sedimentológico de las series del Departamento de Tacna. Tesis de grado. UNSA, Arequipa.

Sánchez-Núñez, J.M., Gómez, J.C., Macías, J.L., Arce, J.L., 2020. Pleistocene rock avalanche, damming, and secondary debris flow along the Cotahuasi river, Peru. J. S. Am. Earth Sci. 104, 102901.

Santibáñez, I., Cembrano, J., García, T., Costa, C., Yañez, G., Marquardt, C., Arancibia, G., González, G., 2019. Crustal faults in the chilean Andes: geological constraints and seismic potential. Andean Geol. 46, 32–65.

Schildgen, T.F., Hodges, K.V., Whipple, K.X., Reiners, P.W., Pringle, M.S., 2007. Uplift of the western margin of the Andean plateau revealed from canyon incision history, southern Peru. Geology 35, 523–526.

Schildgen, T.F., Hodges, K.V., Whipple, K.X., Pringle, M.S., van Soest, M., Cornell, K., 2009. Late Cenozoic structural and tectonic development of the western margin of the central Andean Plateau in southwest Peru. Tectonics 28, TC4007. https://doi.org/10.1029/2008TC002403.

Schildgen, T.F., Balco, G., Schuster, G., 2010. Canyon incision and knickpoint propagation recorded by apatite 4 He/3 He thermochronometry. Earth Planet Sci. Lett. 293, 377–387.

Schmidt, K.M., Montgomery, D.R., 1995. Limits to relief. Science 270 (5236), 617–620.

Sobolev, S.V., Babeyko, A.Y., 2005. What drives orogeny in the Andes? Geology 33 (8), 617–620.

Somoza, R., 1998. Updated Nazca (Farallon) - south America relative motions during the last 40 My: implications for mountain building in the central Andean region. J. S. Am. Earth Sci. 11, 211–215.

Stead, D., Wolter, A., 2015. A critical review of rock slope failure mechanisms: the importance of structural geology. J. Struct. Geol. 74, 1–23.

Steffen, D., Schlunegger, F., Preusser, F., 2010. Late Pleistocene fans and terraces in the Majes valley, southern Peru, and their relation to climatic variations. Int. J. Earth Sci. 99 (8), 1975–1989.

Stirling, M.W., Langridge, R., Benites, R., Aleman, H., 2002. The Magnitude 8.3 June 23 2001 Southern Peru Earthquake and Tsunami: Reconnaissance Team Report. Institute of Geological & Nuclear Sciences.

Strasser, M., Schlunegger, F., 2005. Erosional processes, topographic length-scales and geomorphic evolution in arid climatic environments: the 'Lluta collapse', northern Chile. Int. J. Earth Sci. 94 (3), 433–446.

Strecker, M.R., Alonso, R.N., Bookhagen, B., Carrapa, B., Hilley, G.E., Sobel, E.R., Trauth, M.H., 2007. Tectonics and climate of the southern central Andes. Annu. Rev. Earth Planet Sci. 35, 747–787.

Tanyaş, H., Van Westen, C.J., Allstadt, K.E., Anna Nowicki Jessee, M., Görüm, T., Jibson, R.W., Hovius, N., 2017. Presentation and analysis of a worldwide database of earthquake-induced landslide inventories. J. Geophys. Res.: Earth Surf. 122 (10), 1991–2015.

Tanyaş, H., van Westen, C.J., Allstadt, K.E., Jibson, R.W., 2019. Factors controlling landslide frequency–area distributions. Earth Surf. Process. Landforms 44 (4), 900–917.

Tebbens, S.F., 2020. Landslide scaling: a review. Earth Space Sci. 7 (1), e2019EA000662.

Thouret, J.C., Wörner, G., Gunnell, Y., Singer, B., Zhang, X., Souriot, T., 2007. Geochronologic and stratigraphic constrains on canyon incision and Miocene uplift of the Central Andes in Perú. Earth Planet Sci. Lett. 263, 151–166.

Thouret, J.C., Gunnell, Y., Jicha, B.R., Paquette, J.L., Braucher, R., 2017. Canyon incision chronology based on ignimbrite stratigraphy and cut-and-fill sediment sequences in SW Peru documents intermittent uplift of the western Central Andes. Geomorphology 298, 1–19.

Tomlinson, A., Blanco, N., Ladino, M., 2015. Carta Mamiña, Región de Tarapacá. Servicio Nacional de Geología y Minería, Carta Geológica de Chile. Serie Geología Básica 174, 1 mapa escala 1:100.000. Santiago.

Tonini, M., Pedrazzini, A., Penna, I., Jaboyedoff, M., 2014. Spatial pattern of landslides in Swiss rhone valley. Nat. Hazards 73, 97–110.

Valagussa, A., Marc, O., Frattini, P., Crosta, G.B., 2019. Seismic and geological controls on earthquake-induced landslide size. Earth Planet Sci. Lett. 506, 268–281.

Valdivia-Silva, J.E., Navarro-González, R., Ortega-Gutierrez, F., Fletcher, L.E., Perez-Montano, S., Condori-Apaza, R., McKay, C.P., 2011. Multidisciplinary approach of the hyperarid desert of Pampas de La Joya in southern Peru as a new Mars-like soil analog. Geochem. Cosmochim. Acta 75 (7), 1975–1991.

Valenzuela, J.I., Herrera, S., Pinto, L., Del Real, I., 2014. Carta Camiña, regiones de Arica-Parinacota y Tarapacá. Servicio Nacional de Geología y Minería, Carta Geológica de Chile. Serie Geología Básica 170, 97 pp., 1 mapa escala 1:100.000.

Van Den Eeckhaut, M., Poesen, J., Govers, G., Verstraeten, G., Demoulin, A., 2007. Characteristics of the size distribution of recent and historical landslides in a populated hilly region. Earth Planet Sci. Lett. 256, 588–603.

Varnes, D.J., 1978. Slope movement types and processes. Sp. Rep. 176, 11–33.

Vicente, J.C., 1981. Elementos de la estratigrafía Mesozoica sur Peruana. In: Volkheimer, Musacchio (Eds.), Comité Sudamericano del Jurásico y Cretácico: Cuencas sedimentarias del Jurásico y Cretácico de América del sur, vol. 1, pp. 319–351.

Villegas-Lanza, J.C., Chlieh, M., Cavalié, O., Tavera, H., Baby, P., Chire-Chira, J., Nocquet, J.M., 2016. Active tectonics of Peru: heterogeneous interseismic coupling along the Nazca megathrust, rigid motion of the Peruvian Sliver, and Subandean shortening accommodation. J. Geophys. Res. Solid Earth 121 (10), 7371–7394.

Wallemacq, P., House, R., 2018. Economic Losses, Poverty & Disasters. Centre for Research on the Epidemiology of Disasters and United Nations Office for Disaster Risk Reduction, Geneva, pp. 1–30.

Whipple, K.X., Kirby, E., Brocklehurst, S.H., 1999. Geomorphic limits to climate-induced increases in topographic relief. Nature 401 (6748), 39–43.

Wilson, J., García, W., 1962. Geología de los Cuadrángulos de Pachia y Palca. Comisión de la Carta Geológica Nacional 2 (4), 1–81.

Wörner, G., Hammerschmidt, K., Henjes-Kunst, F., Lezaun, J., Wilke, H., 2000. Geochronology (40Ar/39Ar, K-Ar and He-exposure ages) of Cenozoic magmatic rocks from northern Chile (18-22° S): implications for magmatism and tectonic evolution of the central Andes. Rev. Geol. Chile 27, 205–240.

Wörner, G., Uhlig, D., Kohler, I., Seyfried, H., 2002. Evolution of the West Andean Escarpment at 18 S (N. Chile) during the last 25 Ma: uplift, erosion and collapse through time. Tectonophysics 345 (1–4), 183–198.

Wu, X., Chen, X., Zhan, F.B., Hong, S., 2015. Global research trends in landslides during 1991–2014: a bibliometric analysis. Landslides 12, 1215–1226.

Yilmaz, I., Ercanoglu, M., 2019. Landslide inventory, sampling and effect of sampling strategies on landslide susceptibility/hazard modelling at a glance. In: Natural Hazards GIS-Based Spatial Modeling Using Data Mining Techniques. Springer, Cham, pp. 205–224.

Zavala, B., Mariño, J., Lacroix, P., Taipe, E., Tatard, L., Benavente, C., Pari, W., Macedo, L., Peña, E., Paxi, R., Delgado, F., Fídel, L., Vilchez, M., Gomez, J.C., 2013. Evaluacion de la seguridad fisica del distrito de Maca, Estudio geologicos, geofisicos y monitoreo de movimientos en masa. INGEMMET-IRD-IGP Publications, Lima. Informe Tecnico No. A6628.

Zerathe, S., Lacroix, P., Jongmans, D., Marino, J., Taipe, E., Wathelet, M., Pari, W., Fidel, L., Norabuena, E., Guillier, B., Tatard, L., 2016. Morphology, structure and kinematics of a rainfall controlled slow-moving Andean landslide, Peru. Earth Surf. Process. Landforms 41 (11), 1477–1493.

Zerathe, S., Blard, P.H., Audin, L., Braucher, R., Bourles, D., Carcaillet, J., Benavente, C., Delgado, F., AsterTeam, 2017. Toward the feldspar alternative for cosmogenic 10Be exposure dating. Quat. Geochronol. 41, 83–96.